

**Design and Electromechanical Modeling of Vertically
Stacked Silicon Nanowire Arrays as Coupled Resonators**

by

İsmail Yorulmaz

**A Thesis Submitted to the
Graduate School of Sciences and Engineering
in Partial Fulfillment of the Requirements for
the Degree of**

**Master of Science
in
Materials Science and Engineering
Koç University**

August 2012

Koç University
Graduate School of Sciences and Engineering

This is to certify that I have examined this copy of a master's thesis by

İsmail Yorulmaz

and have found that it is complete and satisfactory in all respects,
and that any and all revisions required by the final
examining committee have been made.

Committee Members:

B. Erdem Alaca, Ph. D. (Advisor)

Arda D. Yalçınkaya, Ph. D.

Ali Serpengüzel, Ph. D.

Date: _____

ABSTRACT

Mechanical resonators are widely used for timekeeping and frequency synthesizing purposes in electronic circuits. Quartz resonators have satisfying performance characteristics like low phase noise and thermal stability. However, micro electromechanical systems (MEMS) resonators are suitable candidates to replace these resonators because of their small size, low power dissipation and relatively low cost due to batch fabrication. For this reason, MEMS resonators have taken part in resonator industry for two decades. Although MEMS resonators are viable candidates, they require further engineering of specifications to match their quartz counterparts. Enhancing the device specification to compete with quartz devices is an intense research subject in the MEMS field.

One of the most important challenges in capacitively transduced micro/nanoresonators is the reduction of the read out signal due to small sizes. In the literature, arraying *i.e.*, summing the outputs of identical resonators was used for increasing the signal for MEMS resonators. For the generation of one mode of vibration from non-identical resonators, mechanical coupling is used. The mechanical resonators at the same plane are placed side by side and connected through mechanical structures, to achieve mechanical coupling.

In this thesis, a novel approach in mechanical coupling was demonstrated for nanowire array resonators, where signal reduction problem becomes more severe. Silicon nanowire (SiNW) resonators, which are vertically arrayed with respect to the substrate, are demonstrated. The mechanical coupling of these nanoresonators is achieved by thin membranes connecting nanowires at both ends. These nanowires are below 50nm in diameter and a few micrometers in length, thus typically generating an operation in high frequency (HF, 3-30MHz), very high frequency (VHF, 30-300MHz) and even in ultra-high frequency (UHF, 300MHz-3GHz) ranges of radio frequency (RF) spectrum.

SiNW array resonators were modeled using equivalent electrical circuits. Electromechanical direct analogy for bending mode clamped-clamped beams was studied to convert mechanical properties into electrical RLC equivalents. Moreover, a modeling procedure related to vertical arraying and mechanical coupling is also demonstrated.

Characterization of SiNWs fabricated by Bosch process was also investigated by fabrication test runs. The outputs of fabrication efforts were directly used as design specifications and fabrication limitations for the modeling of SiNW array resonators.

Furthermore, a full fabrication process including metal electrode formation is also proposed for existing fabrication capabilities.

As a result of these design, fabrication and modeling efforts, some ubiquitous geometries available for fabrication and measurement were determined. Fabrication limitations and need for detectable signals were taken into consideration for designing these geometries.

ÖZET

Mekanik çınlaçlar elektrornik devrelerde yaygın olarak zaman tutma ve sıklık yaratma amaçları için kullanılırlar. Kuvars çınlaçlar ise düşük faz gürültüsü ve yüksek ısıl dengeleri ile tatmin edici başarımlar özellikleri sağlayan mekanik osilatörlerdir. Mikro elektromekanik sistem (MEMS) çınlaçlar ise küçük boyutları, düşük güç tüketimleri ve toplu üretime bağlı düşük maliyetleri ile bu çınlaçların yerini almaya adaydırlar. Bu nedenle, yaklaşık yirmi yıldır MEMS çınlaçlar, salıngaç üretiminde kendilerine yer bulmaktadırlar. Her ne kadar MEMS osilatörler kuvars osilatörlere iyi birer rakip iseler de onları yakalamak için üzerinde daha mühendislik çalışması yapılması gerekmektedir. Kuvars aygıtlarla yarışmak için aygıt özelliklerini geliştirmek ise, MEMS alanında yoğun uğraşın olduğu bir araştırma alanıdır.

Sığa ile tahrik edilip sığa ile okuma gerçekleştirilen mikro/nanoçınlaçların en büyük sorunlarından birisi düşük boyutlara bağlı olarak okuma iminin azalmasıdır. Literatürde *dizileme*, yani birbirine eş çınlaçların çıkışlarını toplayarak sinyali artırma ise MEMS çınlaçlar için kullanılan bir yöntemdir. Birbirine eş olmayan çınlaçların tek bir titreşim kipi ortaya koyması için de mekanik bağlaşma kullanılmaktadır. Mekanik çınlaçlar aynı düzlemde yan yana dizilerek birbirlerine mekanik yapılarla bağlanırlar ve bu sayede mekanik bağlaşma gerçekleşmiş olur.

Bu tez, mekanik bağlaşmayı, im sönümünün önemli olduğu nanotel çınlaç dizilerine uygulayarak yeni bir yaklaşım getirmektedir. Burada, üst üste, alttaki tabakaya dik olarak dizilene silisyum nanotel (SiNT) çınlaçlar gösterilmiştir. Bu nanoçınlaçların mekanik bağlaşması ise nanotelleri her iki ucundan bir diğerine bağlayan ince zar yapılarla sağlanmıştır. Bu nanotellerin çapı 50 nm'den küçük, boyları ise birkaç mikrometre uzunluktadır. Böylece genellikle radyo sıklığının yüksek sıklık (HF, 3-30MHz), çok yüksek sıklık (VHF, 30-300MHz) ve ultra-yüksek sıklık (UHF, 300MHz-3GHz) aralıklarında çalışma sıklığı sağlamaktadırlar.

SiNT dizi çınlaçların eşdeğer elektrik devreleri ile gösterimleri yapılmıştır. Çift taraflı tutturulmuş eğilme hareketi yapan çubuklar için elektromekanik doğrudan benzetim (direct analogy) çalışılarak bunların mekanik özellikleri RLC eşdeğerlerine dönüştürüldü. Ayrıca, üst üste dizileme ve mekanik kuplaja yönelik bir modelleme izleği de gösterildi.

Bosch süreci sonucunda üretilen nanotellerin incelemesi de üretim çalışmaları ile yapıldı. Bu üretim çabalarının sonuçları ise doğrudan tasarım değerleri ve üretim

kısıtlamaları olarak SiNT dizi ınlalarının modellenmesinde kullanıldı. Bunun dıřında metal elektrot oluřumunu ieren, gncel retim olanakları dřnlerek eksiksiz bir retim sreci de nerilmektedir.

Bu tasarım, retim ve modelleme alıřmalarının bir sonucu olarak retime ve lme uygun tasarımlar belirlenmiřtir. Bu yapıları tasarlarken de retim kısıtlamaları ve llebilir im gereksinimleri gz nnde bulundurulmuřtur.

ACKNOWLEDGEMENTS

I would like to thank my thesis advisor Dr. Erdem Alaca for giving me the opportunity to work with him. I am also grateful to Dr. Arda D. Yalçinkaya for his guidance and help about my circuit simulations. I would also like to thank Prof. Ali Serpengüzel for the time he spent during the evaluation of my thesis and progress.

I would also like to thank my group mate Berkay Gümüş not only carrying out fabrication test runs, but also for the fruitful discussions we had. I would like to thank my other group mates Zuhale Taşdemir, Yasin Kılınç and Gökhan Nadar for their sincere friendship and help throughout my Master of Science study.

Other than friends in my group, I would like to thank Mustafa Eryürek, İşinsu Baylam, Ayşen Sarıoğlu, Mine Toker, Orkun Önal, Erhan Atçı, Evren F. Arkan and my other friends that I am fortunate to meet at Koç University.

Lastly, I owe a lot to my family for their love and support and being there whenever I was in need, especially to my brother Mustafa Yorulmaz for his invaluable support throughout my life and to my father for his endless patience and support. This thesis is dedicated to my father, Abdullah Yorulmaz.

This thesis was supported in part by TÜBA-GEBİP and Koç University-İstanbul Rotary Club Fundamental Research Seed Fund Program.

TABLE OF CONTENTS

Chapter 1: INTRODUCTION	1
1.1 MECHANICAL RESONATORS	1
1.2 ACTUATION TECHNIQUES FOR NANOWIRE RESONATORS.....	6
1.2.1 Electrostatic Actuation.....	6
1.2.2 Magnetomotive Actuation	8
1.3 DETECTION TECHNIQUES FOR NANOWIRE RESONATORS	9
1.3.1 Capacitive Detection.....	9
1.3.2 Optical Detection	11
1.3.3 Piezoelectric and Piezoresistive Detection	13
1.3.4 Magnetomotive Detection.....	13
1.4 SILICON NANOWIRE ARRAY RESONATORS	14
Chapter 2: NANOWIRE ARRAY AS A COUPLED RESONATOR	16
2.1 Arraying and Mechanical Coupling	16
2.2 Micro and Nanomechanical Resonators Field with Mechanical Coupling.....	18
2.3 Mechanical Coupling in Vertically Stacked Silicon Nanowire Resonators.....	19
Chapter 3: COUPLED NANOWIRE ARRAY RESONATORS	21
3.1 Electromechanical Analogies	21
3.3 Equivalent Circuit Modeling of Coupled Array resonators	28
Chapter 4: FABRICATION	33
4.1 Process Flow	33
4.2 Proposed fabrication flow	36
Chapter 5: CONCLUSION	39
Chapter 6:OUTLOOK	41
Appendix A:Calculation of RLC	47
Appendix A:MATLAB Code	50
Appendix B:COMSOL Multiphysics: Electrostatic Module Simulations	54

LIST OF TABLES

<i>Table 1.1 Literature on clamped-clamped silicon nanowire resonators with various actuation and detection methods.</i>	<i>4</i>
<i>Table 1.2 Clamped-clamped nanowire resonator literature with electrostatic actuation. ...</i>	<i>7</i>
<i>Table 1.3 Clamped-clamped nanowire resonator literature with magnetomotive actuation.</i>	<i>9</i>
<i>Table 1. 4 Clamped-clamped nanowire resonator literature with capacitive detection.</i>	<i>11</i>
<i>Table 1.5 Clamped-clamped nanowire literature with optical detection.</i>	<i>12</i>
<i>Table 1.6 Clamped-clamped nanowire literature using magnetomotive detection.</i>	<i>14</i>
<i>Table 3.1 Effort-flow relations of electrical and mechanical energy domains.</i>	<i>22</i>
<i>Table 3.2 Connection rules for mechanical and electrical networks.</i>	<i>24</i>
<i>Table 3.3 Silicon nanowire resonator design and parameter summary.</i>	<i>26</i>
<i>Table 3.4 Nanowire resonator parameter summary for coupled array simulations.</i>	<i>31</i>
<i>Table 4. 1 The recipe of Bosch process ZZ_SOI_accu2 for nanowire fabrication.</i>	<i>35</i>
<i>Table 6.1 Nanowire resonator parameter summary for 1.8μm-long nanowire array simulations.</i>	<i>42</i>
<i>Table 6.2 Nanowire resonator parameter summary for 1.5μm-long nanowire array simulations.</i>	<i>43</i>
<i>Table 6.3 Nanowire resonator parameters for 1μm-long nanowire array simulations</i>	<i>44</i>
<i>Table 6.4 Nanowire resonator parameters for 750nm-long nanowire array simulations. .</i>	<i>45</i>
<i>Table 6.5 Nanowire resonator parameters for 500nm-long nanowire array simulations ..</i>	<i>46</i>

LIST OF FIGURES

<i>Fig.1.1 One of the first miniaturized resonators used for frequency selection in transistors[5].</i>	2
<i>Fig.1.2 A basic scheme of electrostatically actuated double clamped nanowire resonator.</i>	7
<i>Fig.1.3 A basic scheme of magnetomotive transduction, in plane with the detection electrode.</i>	8
<i>Fig.1.4 A typical capacitive detection scheme for nanowire resonators.</i>	10
<i>Fig.1. 5 Common detection schemes for optical detection of nanowire resonators. a)Fabry-Perot type detection scheme and b)Michelson type interferometric detection scheme [32].</i>	12
<i>Fig. 2.1 Nanowire resonators having about 5% frequency mismatch result in decoupling.</i>	17
<i>Fig. 2.2 Signal outputs of single, two coupled and four coupled nanowire resonators. Inset shows the same graph with output axis in logarithmic scale.</i>	17
<i>Fig. 2.3 Side view of the vertically stacked nanowire array resonators.</i>	19
<i>Fig. 2.4 a) Crystal orientation of a (100) silicon wafer. b) Directions and axes in a (100)wafer</i>	20
<i>Fig 3.1 Equivalent RLC circuit of the lumped mass stiffness damper model in direct analogy.</i>	23
<i>Fig 3.2 a) Top view of the nanowire resonator layout including ac and dc voltages and read out nodes. b) Electrical equivalent circuit of this layout with input/output capacitances and resistances which are typically 50Ω. c) Electrical equivalent circuit of the same with transformer model.</i>	25
<i>Fig 3.3 SPICE equivalent circuit model result of Design 1.</i>	27
<i>Fig 3.4 SPICE equivalent circuit model result of Design 2.</i>	27
<i>Fig 3.5 Four mode shapes and eigenfrequencies of coupled array resonators demonstrated by COMSOL Multiphysics.</i>	29
<i>Fig 3.6 Summary of the modeling procedure for single and coupled array nanowire resonators.</i>	30
<i>Fig 3.7 SPICE equivalent circuit model result of array resonators.</i>	31

Fig 3.8 SPICE circuit equivalent for four coupled nanowire resonators geometries of which are given in Table 3.3.	32
Fig. 4. 1 Process flow for the fabrication of silicon nanowire array (a) wafer preparation, (b) e-beam lithography, (c) Bosch process, (d) HF vapor e-beam resist removal.	34
Fig. 4. 2 A 2.5 μm -long nanowire array SEM image.	34
Fig.4.3 A 1.8 μm -long nanowire array SEM image before e-beam resist removal.	35
Fig.4.4 500nm-long silicon nanowire array field emission SEM image after e-beam resist removal.	36
Fig. 4. 5 Proposed process flow for silicon nanowire resonators with metal electrodes. ..	38
Fig.6.1 SPICE equivalent circuit model signal output of 1.8 μm -long nanowire array resonators.	42
Fig.6.2 SPICE equivalent circuit model signal output of 1.5 μm -long nanowire array resonators with $Q=7500$	43
Fig.6.3 SPICE equivalent circuit model signal output of 1 μm -long nanowire array resonators with $Q=15000$	44
Fig.6.4 SPICE equivalent circuit model signal output of 750nm-long nanowire array resonators with $Q=750$	45
Fig.6. 5 SPICE equivalent circuit model signal output of 500nm-long nanowire array resonators with $Q=750$	46
Fig. A.1 Resonator cross-sectional schematic for frequency pulling and impedance analysis.	48
Fig. A. 2 Clamped-clamped beam micromechanical resonator typical excitation configuration.	48
Fig.B.1 Cross- sectional view of the structures drawn in COMSOL for capacitance simulation.	54
Fig.B.2 COMSOL screen print for calculation of electrode to resonator capacitance.	55
Fig.B. 3 A typical configuration of probes during measurement.	55

Chapter 1

INTRODUCTION

1.1 MECHANICAL RESONATORS

Resonators serving as frequency references form the basis of almost all electronic devices. They provide precision in the timescale to the electronic circuits. Oscillators can be all-electronic such as RC or LC-based complementary metal-oxide-semiconductors (CMOS) oscillators, or can be electromechanical like quartz, converting mechanical energy to electrical energy. Oscillators are used to generate signals at a precise frequency. A quartz watch counts time using the precise frequency generated by quartz oscillators.

Major types of mechanical oscillators include quartz or other piezoelectric crystals. The current high-Q resonators are surface acoustic wave (SAW), film bulk acoustic wave (FBAR) and quartz tuning forks, which are all basically electromechanical elements converting mechanical energy to electrical energy and hence generate signals with desired frequency or filtering characteristics [1]. The ultimate choice of materials is based on cost and application-dependent performance requirements.

Quartz provides best performance in terms of stability at highest cost. Quartz crystal has been used for timekeeping purposes since as early as 1940s. Quartz is today used for high-precision applications such as wireless communication. Quartz is especially advantageous due to its high thermal stability and low power dissipation [2, 3].

However, such crystal oscillators come in relatively large sizes leaving little room for miniaturization. Furthermore, their processing and integration with other microsystems or electronics is not batch compatible leading to another and even more serious barrier to miniaturization. The latter means extra board-level integration with additional electronics to implement the desired use. The usage of such extra electronics increases overall cost in addition to power consumption as well as noise level.

Micro electromechanical systems (MEMS) oscillators form the other alternative for mechanical oscillators. They are based on a miniature resonating mass made up of usually

silicon or similar material. Efforts for miniaturization of mechanical oscillators date back to 1960s. The first microscale resonating bodies were microcantilevers that are suggested as frequency selectors in integrated circuits [4]. First resonant gate transistors (RGT) offered substantial size reductions for the frequency selecting circuit elements. However, the lack of microfabrication techniques for building RGTs caused fatigue and a Q-factor ranging between hundred to several hundred [4, 5]. Moreover, since the resonating body is miniaturized, the damping of air molecules became severe, and the necessity of hermetic sealing arose in order to reduce the damping, which is also a current issue in MEMS resonator field [2, 5]. Another current issue is temperature instability, which is compensated with on-chip digital tuning. This tuning also leads to the phase noise of the oscillator [2].

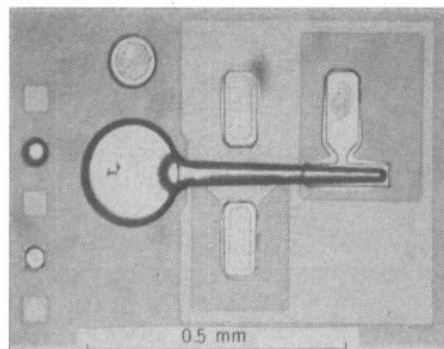


Fig.1.1 One of the first miniaturized oscillators used for frequency selection in transistors[5].

Recently, microresonators facilitated miniaturization and a high level of integration, due to the batch compatibility and use of conventional microfabrication techniques. Today, quality factors beyond 10^6 are already reported [3]. Recent advances in microfabrication technology also made them more practical even for the commercial applications. For this reason, MEMS oscillators took place in the market for more than a decade. The vendors currently supplying MEMS oscillator to the market are Abracon, Discera, Ecliptek, IDT, IQD, NXP, Sand9, Silicon Labs, SiTime, TXC Corporation [6]. Oscillators represent a multibillion-dollar market, in which MEMS oscillators hold less than one percent share. MEMS market is expected to reach \$312 million by 2014 [6].

One of the most promising applications of MEMS oscillators is in filtering. MEMS filters are basically mechanical resonators, in which the signal is engineered by using various mechanical (acoustic) coupling elements. Early macroscopic mechanical filters and

their design with different coupling beams can be modeled by equivalent circuit modeling methods. The mechanical coupling in these macroscopic resonators is obtained by coupling wires with diameters in the millimeter range[7]. The same approach for equivalent circuit modeling is adopted in their current MEMS counterparts. Equivalent circuit modeling provides successful design of desired filter element. (Butterworth, Chebyshev, etc.) Once the equivalent circuit is obtained, it is possible to observe the signaling behavior of the electromechanical element. The ability to predefine the mode of operation of coupled oscillators makes them suitable candidates for replacing other kinds of electronic filters.

The miniaturization of resonators continues into the nanoscale, which provides a higher frequency and resolution in general. Recently, even yoctogram (10^{-24} g) resolution mass sensors are achieved vibrating at almost 2 GHz by facilitating nanoscale resonating bodies [8]. This kind of achievements shows the trend of technology is to achieve higher resolution in sensing and higher operation frequency, which is made possible by nanoscale engineering.

In order to carry out this miniaturization effort explained above from microscale to nanoscale for frequency synthesizing mechanical devices, bending mode clamped-clamped (CC) silicon nanowire resonators were utilized along with other nanoscale resonators. In Table 1.1, the studies on silicon nanowire resonators are listed with dimensions, applications and fabrication methods of these devices.

Achieving nanoscale resonator devices allows higher operation frequency, higher sensitivity for sensors, and minimum device size. However, the disadvantages that show up in the microscale like air damping and temperature instability might be more severe for nanoresonator.

Table 1.1 Literature on clamped-clamped silicon nanowire resonators with various actuation and detection methods.

Length×width×height ($\mu\text{m} \times \text{nm} \times \text{nm}$)	Resonance Freq. (MHz)	Q Factor	Applications/ Significance	Fabrication Method	Ref.
2 × 100 × 100.	225	$\approx 10^3$	Potential sensing application	e-beam, evaporation&liftoff of Cr or Al, RIE, wet etch, evaporation of Cr&Au	[9]
2 × 100 × 200	380	$\approx 10^3$	Potential sensing application	e-beam, evaporation&liftoff of Cr or Al, RIE, wet etch, evaporation of Cr&Au	[9]
3 × 200 × 250	37.26	2330	Potential nonlinear oscillators for SPM	e-beam, Au/Al deposition, RIE, wet etch	[10]
40 μm × 3 μm	≈ 10	2400	Potential MEMS filter to be used in wireless applications	THELMA(Thick Epi-Poly Layer for Microactuators and Accelerometers) an industrial Bosch process min. feature size 2 μm	[11]
24 μm ×2 μm	31.6	2500	Potential for sensors	LPCVD carrier doping, Plasma etch,RIE LPCVD of poly	[12]
10 μm ×150nm	14.8	NA	Potential sensing application	Metal-catalyzed chemical vapor deposition (MCCVD),Self Welding	[13]
6 μm ×1 μm	18.9 (1 st)	30	Photothermal operation	NA	[14]
2×165×125	145	400	Sensor in air and liquid	e Beam,RIE(CHF3/O2 plasma), wet etch	[15]
1.69 μm ×81nm	215	≈ 2000	Potential resonant sensor	VLS epitaxial growth self welding	[16]
2.77 μm ×74nm	80	≈ 13100	Potential resonant sensor	VLS epitaxial growth self welding	[16]
7.92 μm ×526nm	5.01	3.9	Potential for ultralow power applications	i-line Photolith., RIE, Wet etch,	[17]

Length×width×height ($\mu\text{m} \times \text{nm} \times \text{nm}$)	Resonance Freq. (MHz)	Q Factor	Applications/ Significance	Fabrication Method	Ref.
17.7 μm ×175nm	533	7500	Potential for sub aN force sensitivity meas.	VLS	[18]
4.9 μm ×88nm &4.6 μm ×80nm	22&29.9	800	Potential for integrated NEMS	Photolith., VLS,CVD,	[19]
2-20 μm ×39-400nm	1-12	5-25 $\times 10^3$	Potential for sensors	VLS	[20]
10×165 ×120	14.3	NA	Measurement via CMOS integration	NA	[21]
5 μm ×300nm	19.6	200	Potential for mass detection	E beam/DUV lith., RIE, vapor HF etching	[22]
6 μm ×400nm	70	2900	Resonant Body FET	E beam, wet etch	[23]
3×140×200	80	1100	Resonant Body FET	E beam, wet etch	[23]

1.2 ACTUATION TECHNIQUES FOR NANOWIRE RESONATORS

Bending mode double clamped nanowire or nanobeam resonators in the literature were driven basically with electrostatic and magnetomotive actuation. The corresponding literature with their use of such actuation techniques are the following.

1.2.1 Electrostatic Actuation

Operation principle of electrostatic actuation systems emerges from the Coulomb force between opposite charges on the gate electrode and the beam. General electrostatic actuation scheme for the clamped clamped nanowire resonators is shown in Fig.1.2. Neglecting the fringing fields and having parallel plate capacitor scheme system in Fig.1.2 will have energy:

$$E = \frac{1}{2} \frac{CV^2}{d} = \frac{1}{2} \frac{\epsilon_0 AV^2}{d} \quad 1.1$$

where, C is capacitance between parallel plates, A is intersecting area, d is distance between the plates and V is the electrical potential difference between the plates. The force becomes:

$$F = \frac{\partial E}{\partial d} = \frac{1}{2} \frac{\epsilon_0 AV^2}{d^2} \quad 1.2$$

Typically applied voltage (V) becomes a combination of an ac voltage ($V_{ac} \sin \omega t$) with a dc bias (V_{dc}): $V = V_{dc} + V_{ac} \sin \omega t$. In this configuration, the force exerted from actuation electrode will be:

$$F = \frac{\epsilon_0 hl (V_{dc}^2 + 2V_{ac}V_{dc} \sin \omega t - V_{ac}^2 (\sin \omega t)^2)}{2d^2} \quad 1.3$$

h and l corresponds to height and length of the nanowire. Using double angle formula for the cosine and factoring out V_{ac} , one will have:

$$F = \frac{\epsilon_0 hl V_{ac}^2 \left(\left(\frac{V_{dc}}{V_{ac}} \right)^2 + \frac{1}{2} + 2 \frac{V_{dc}}{V_{ac}} \sin \omega t - \frac{1}{2} \cos 2\omega t \right)}{2d^2} \quad 1.4$$

For the case with no dc bias, the cosine term dominates the equation and hence the ac drive frequency (ω_{ac}) should be the half of the natural frequency of the nanoresonator (ω_{res}) to achieve resonant vibration. ($2\omega_{ac} = \omega_{res}$). For the ac drive with dc bias, the sine term will dominate and the drive frequency should be tuned to exact natural frequency of

the nanowire [24]. Here, we have basically three force component contributing to actuation of nanowire, including, a dc term at 0 Hz, a term at ω_{ac} and a term at $2\omega_{ac}$. Thus, the nonlinearity of the system is stem from this relation.

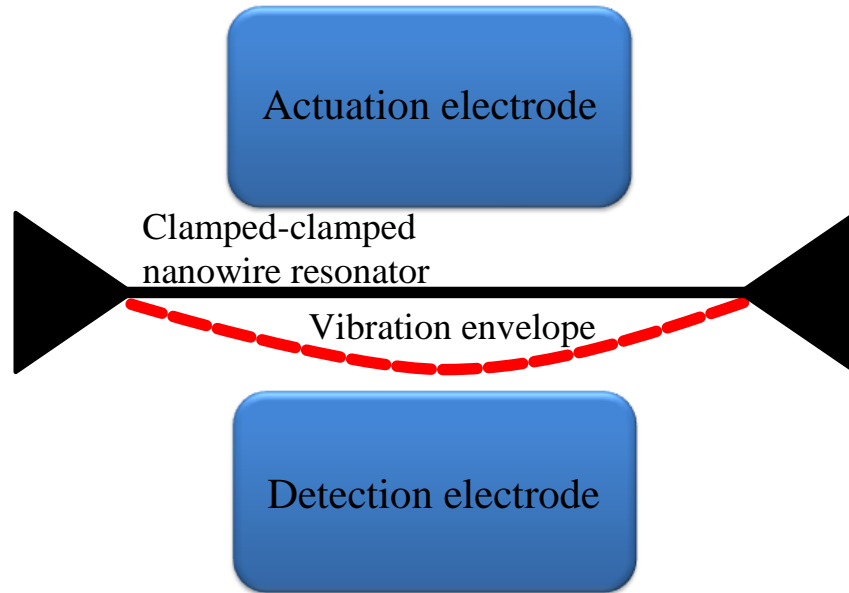


Fig.1.2 A basic scheme of electrostatically actuated double clamped nanowire resonator.

Table 1.2 Clamped-clamped nanowire resonator literature with electrostatic actuation.

Vibrating Material	Length×width×height	Resonance freq. (MHz)	Quality factor	Resonator gap	Bias Voltage (V)	Ref
Si	2 μm ×100 nm×200nm.	380	$\approx 10^3$	400nm	NA	[9]
Si	40 μm ×3 μm	9.98	2400	0.57 μm	40	[11]
Si	10 μm ×165nm	14.3	NA	120nm	NA	[21]
ZnO	12 μm ×500nm	21	NA	340nm	0.2	[25]
Si	10 μm ×400nm×200nm	27.6	150	300nm	2	[26]
ZnO	1.91 μm ×10nm	21.4	242	100nm	2	[27]
Polysilicon +Metal	8.6 μm ×270nm	26	42	280nm	80	[28]
Polysilicon +Metal	2.7 μm ×300nm	234	145	280nm	80	[28]
Si	2.5 μm ×80nm	94.7	NA	120nm	0.800	[29]
Al	3 μm ×147nm	101.3	NA	29nm	NA	[30]
Si ₃ N ₄	1to8 μm ×50-300nm	29-171	2000-2500	NA	NA	[31]

This method provides simplicity in the experimental setup since it does not require cryostat and magnetic fields which requires extra endeavor to induce. Also it is advantageous for everything needed for operation is ubiquitous on the scheme. This makes it invaluable for integration with CMOS. For this reason most of the endeavor in nanowire resonator study utilizes electrostatic actuation. In Table 1.2, nanowire resonator literature utilizing electrostatic actuation methods is listed.

1.2.2 Magnetomotive Actuation

The magnetomotive motion of nanowire is generated by utilization of Lorentz force. An AC current is passed through the beam with a magnetic field perpendicular to the beam. (Fig.1.3) This way, an electromotive force of magnitude $F(\omega) = lBI(\omega)$ is applied to the beam in the in plane or out of plane direction, where $I(\omega)$ is the magnitude of the current applied to the beam and l is the length of the nanowire [32].

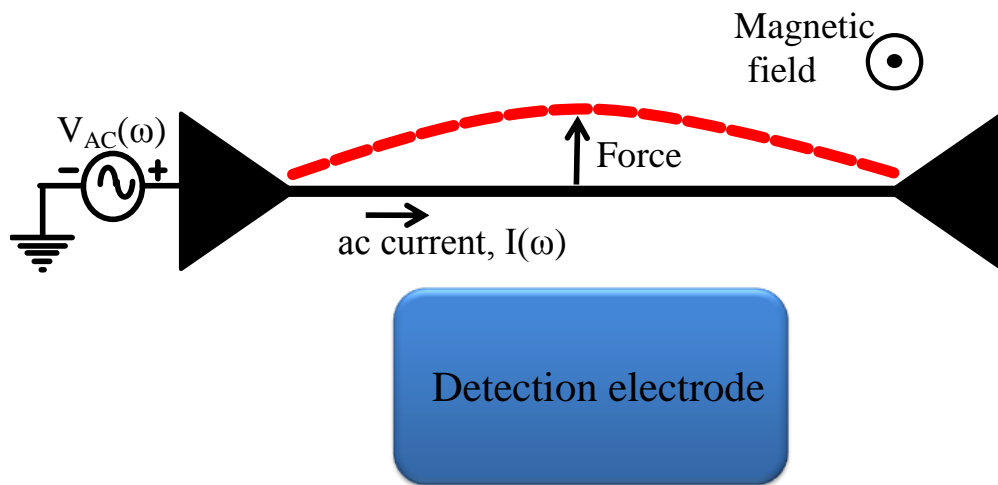


Fig.1.3 A basic scheme of magnetomotive transduction, in plane with the detection electrode.

Although NEMS operating at 1GHz was demonstrated, the technique requires strong magnetic fields, usually on the order of Teslas [32]. Moreover, this technique usually requires vacuum and/or cryostats. This makes the method harder to implement and impossible to device-level integration. Nanowire resonator literature utilizing magnetomotive actuation is listed in Table 1.3.

Table 1.3 Clamped-clamped nanowire resonator literature with magnetomotive actuation.

Material	Length×width×height	Resonance freq. (MHz)	Quality factor	Ref
Au/Si	3 μm×200nm×250nm	37.26	2330	[10]
Si	10μm×150nm	14.8	NA	[13]
Si	1.69μm×81nm	215	≈2000	[16]
Si	2.77μm×74nm	80	≈13100	[16]
Si	7.7μm×330nm×800nm	70.72	20000	[33]
GaAs	3μm×250nm×200nm	116.7	≈1700	[34]

1.3 DETECTION TECHNIQUES FOR NANOWIRE RESONATORS

Detection techniques for double clamped nanowire formation are various including magnetomotive, capacitive, piezoelectric, piezoresistive methods and interferometry [32]. In this section, some state of the art examples of these techniques are introduced.

1.3.1 Capacitive Detection

In capacitive detection, the oscillatory motion of the mechanical element is detected by the change of capacitance between the vibrating element, and a nearby gate electrode (Fig.1.4). The vibration of the nanowire creates a disturbance in the electric field. This periodic disturbance due to vibration is detected as an induced current or transmission by the nearby detection electrode.

The total detected induced current, I on the electrode stems from feed through capacitances between the electrodes, C_f and motional capacitance change, ΔC :

$$I = I_f + I_m = C_f \frac{\partial V_{ac}}{\partial t} + (V_{dc} + V_{ac}) \frac{\partial \Delta C}{\partial t} \quad 1.5$$

Here I_f is the feed through current induced by the ac drive voltage and I_m is the motional current induced by the vibration of the electrode. For the case in which there is no dc bias, the induced current becomes;

$$I = I_f + I_m \cong C_f \frac{\partial V_{ac}}{\partial t} + V_{ac} \frac{\partial \Delta C}{\partial t} \quad 1.6$$

This equation results a feed through current, since in general, $\Delta C \ll C_f$. For the case, when $V_{dc} \gg V_{ac}$, the equation becomes:

$$I = I_f + I_m \cong C_f \frac{\partial V_{ac}}{\partial t} + V_{ac} \frac{\partial \Delta C}{\partial t} \quad 1.7$$

In the literature, the current obtained from a grounded setup (Eq. 1.6) is subtracted from dc biased signal (Eq. 1.7), in order to eliminate the feed through signal [24].

Although it is not easy to use capacitive detection schemes at nanoscale since the signal level is challenging to detect, capacitive actuation is quite common for nanomechanical resonators. The main drawback of this technique is the existence of considerable parasitic coupling of the gate electrode and hence detecting the small capacitance change embedded in this parasitic capacitance, due to the motion of the beam. For example, a 12 μm long metallic gate separated by 100nm will have a static capacitance of 10^{-17} F at 10-100MHz, where its capacitance change due to the motion of the nanowire is 10^{-19} F [35]. However, the structural requirements of capacitive technique are limited that electrodes nearby the resonator for actuation and read out functions suffice. As a result of this simplicity it promises high level integration whereas other methods such as optical and magnetomotive readout are impossible to integrate at device level. The nanowire literature utilizing capacitive detection is listed in Table 1. 4.

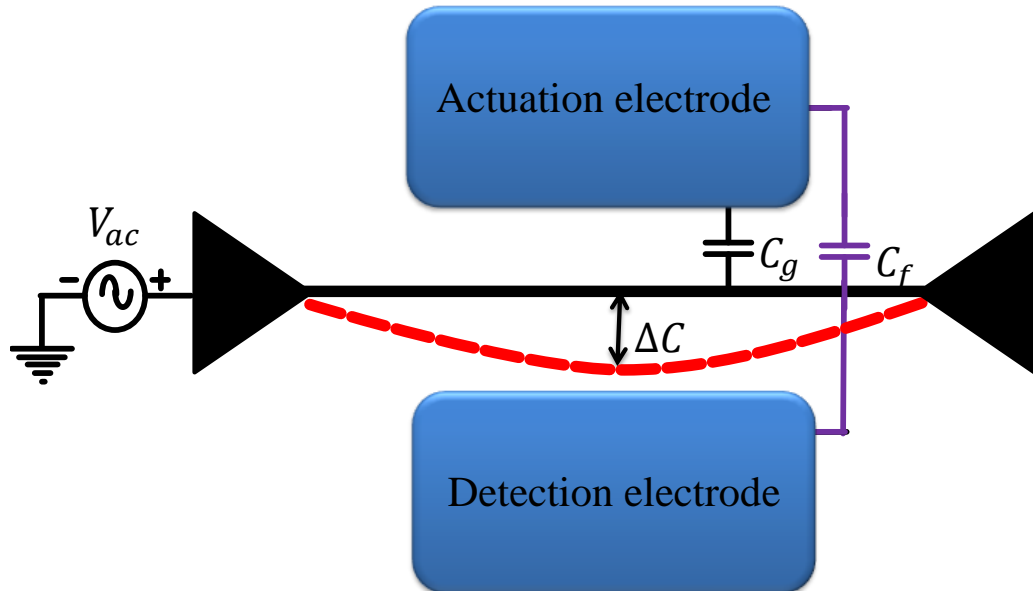


Fig.1.4 A typical capacitive detection scheme for nanowire resonators.

Table 1. 4 Clamped-clamped nanowire resonator literature with capacitive detection.

Material	Length×width×height	Gap (nm)	Displacement sensitivity (pm/\sqrt{Hz})	Resonance Freq. (MHz)	Quality Factor	Ref.
Si	3 μm ×200 nm ×250nm	NA	NA	37.26	2330	[10]
Si	40 μm ×3 μm	Tunable	NA	10	NA	[11]
Si	10 μm ×165nm ×120nm(d)	100	NA	14.3	NA	[21]
Al on Si ₃ N ₄	12 μm ×200nm×150nm	180	4.1 @V _g =15V	11.2	26500@4.2K	[35]
Al on Si ₃ N ₄	14 μm ×200nm×205nm	130	4.1 @V _g =15V	13.5	1800	[35]
Si ₃ N ₄	30-40 μm ×200nm×100nm	300	20	5-9	100×10 ³ -150×10 ³	[36]
GaAs	3 μm ×250nm×200nm	250	0.002	116	1700@30mK	[34]
Metal	2.7 μm ×300nm	280	NA	228	145	[28]
SiC	3 μm ×55nm×50nm	90	NA	70.4	1825	[37]
SnO ₂	L=1.5-3 μm	NA	NA	59	2200	[38]
Al	4 μm ×125nm×141nm	29	NA	101	270×10 ³ @25mK	[30]

1.3.2 Optical Detection

The most common optical detection method in nanowire resonators is interferometry. Basically two types of interferometry are used in detection of fundamental frequency and displacement of nanoscale resonator. In Fabry-Perot interferometry, the light reflected from resonator surface is modulated by the vibration and this light interferes with the light reflected from the substrate. In Michelson interferometer, the incident beam is split using a beam splitter and interference takes place between the reference light beam obtained from the beam splitter (BS) and the light reflected from the resonator surface. The change in light intensity due to oscillation of the nanowire is detected by the change of photocurrent on a photodiode (PD) for both detection techniques.

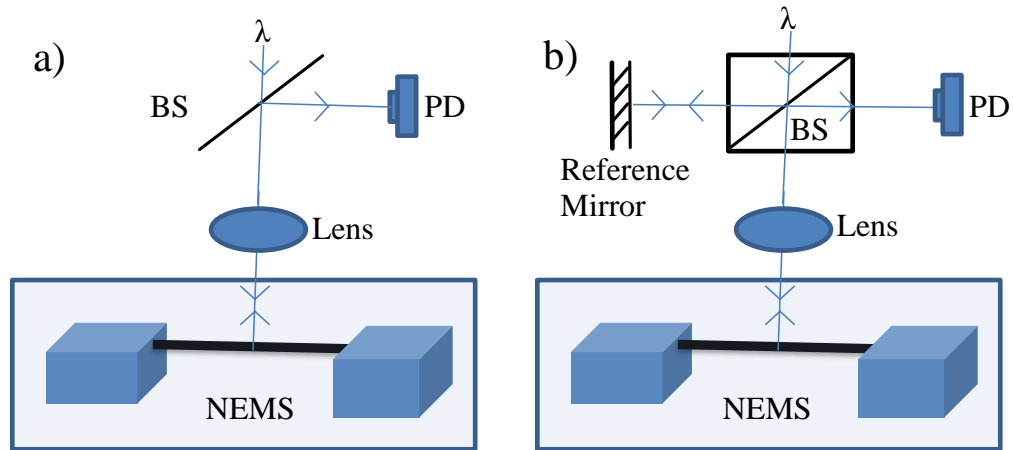


Fig.1. 5 Common detection schemes for optical detection of nanowire resonators. a) Fabry-Perot type interferometric detection scheme and b) Michelson type detection scheme [32].

The advantage of using optical detection techniques is basically based on its successful operation at room temperature detection. However, the sensitivity of the optical detection techniques is limited by diffraction which makes it challenging for nanoscale resonator detection. Moreover, the interference techniques do not provide chip level integration and hence not promising for device-level applications. Examples of such optical detection techniques for clamped-clamped nanowire resonators are listed in Table 1.5.

Table 1.5 Clamped-clamped nanowire literature with optical detection.

Material	Length/width×height	Displacement Sensitivity (pm/\sqrt{Hz})	Resonance Freq. (MHz)	Quality factor	Ref.
Si	2 μm /200 nm×100nm.	NA	380	$\approx 10^3$	[9]
Cr on Si	6 μm /1 μm ×250nm	NA	18.9	≈ 30	[14]
Si	2 μm /165nm×125nm	NA	145	400	[15]
Si	17.7 μm /175nm	0.5	0.533	7500	[18]
Si (cantilever)	5.2 μm /40nm	NA	1.84	≈ 4200	[20]
Si ₃ N ₄	35 μm /100nm×200nm	1	10	10^5 @10^{-4} mbar	[39]
Si	10 μm /220nm×400nm	0.050-0.350	27.6	150	[26]
Si ₃ N ₄	14 μm /200nm×125nm	NA	7-20	800	[40]

1.3.3 Piezoelectric and Piezoresistive Detection

A piezoelectric material exhibits an electrical polarization due to an applied strain. A piezoresistive material exhibits a change in its resistivity due to applied strain. Thus, both methods utilize the electrical property change in the material due to applied strain rather than directly measuring the displacement. Since the resistance change is small for nanoscale resonators it is hard to detect this strain for the piezoresistive method. Similarly, the piezoelectric potential generated by strain in a nanoresonator will be very small. These problems are awaiting for successful detection solutions for the piezoelectric and piezoresistive case. Moreover, since it is an indirect method, it still does not provide displacement detection which is important for realization of device operation. However, if these problems overcome, it will provide high level integration using its electrical detection either piezoelectric or piezoresistive. Piezoelectric and piezoresistive based detection methods are not widespread in nanoelectromechanical systems (NEMS) field for the above mentioned problems, and there is no clamped-clamped nanowire resonator detection is announced to the date.

1.3.4 Magnetomotive Detection

In magnetomotive detection, a conducting nanoresonator vibrates in a static magnetic field and thus generates an electromotive force (emf), which can be detected by a readout circuit. For a magnetomotive actuation scheme seen in Fig.1.3 electromotive force generated is

$$v_0(t) = 0.885lBv(t) \quad 1.8$$

where, l is length of the beam, B is magnetic field, $v(t)$ is time dependent velocity of the midpoint of the beam and 0.885 is the geometrical factor used for double clamped beams [32].

Magnetomotive detection is popular for detection of nanoelectromechanical systems (NEMS). In most of the cases the signal is amplified using an amplifier since NEMS will result in small displacements and low signals. The corresponding nanowire literature with magnetomotive readout is given in Table 1.6.

Table 1.6 Clamped-clamped nanowire literature using magnetomotive detection.

Material	Length/diameter	Detection Efficiency (SBR: signal to background ratio)	Resonance Freq. (MHz)	Quality factor	Ref.
Si	10 μ m \times 150nm	NA	14.8	NA	[13]
Al&Ti on Si	L=2.25 μ m, d=142 nm	SBR \approx 8.5dB @B=8T	200	2000 @25K@vacuum	[16]
Al&Ti on Si	L=2.1 μ m, d=118nm	SBR \approx 12.5dB @B=8T	188	2500 @25K@vacuum	[16]
Si	L=1.69 μ m, d=81nm	SBR \approx 0.8dB	215	5750	[16]
Si	L=2.77 μ m, d=74nm	SBR \approx 1.6dB	80	13100	[16]
Pt	L=1.3 μ m, d=43nm	NA	105.3	8500@4K	[41]

1.4 SILICON NANOWIRE ARRAY RESONATORS

Our study aims an electrostatic transduction method in which actuation and detection both depend on capacitive phenomena. Although lower signal level at nanoscale makes it hard to detect it, is a common problem for all kind of transduction methods at this scale. Moreover, electrostatic transduction method requires only electrodes nearby the resonator for actuation and detection purposes. Yet, magnetomotive and optical detection techniques have requirements beyond chip level such as a magnetic field on the order of Tesla and a laser beam makes their integration quite problematic for the state of the art technologies. For this reason capacitive transduction methods are the most common in the MEMS resonators.

In order to enhance the signal level for capacitive transducers, it is useful to reduce the electrode to resonator gap, increase the dc polarization voltage and/or sum the outputs of the identical resonators [42]. Although first two are very effective techniques, they suffer from nonlinearity. Arraying resonators is found to be quite useful and is used in the literature to increase the read out signal[42]. Since small structural differences from one resonator to another causes different operation frequencies, the resonators are mechanically coupled to each other to generate a single mode of vibration. All the work on mechanically

coupled array resonators focuses on planar processing technologies *i.e.*, resonators are placed horizontally next to each other and coupled through other horizontally placed elements and hence they suffer from growth of overall oscillator size almost proportional to the number of resonators.

In order to enhance the signal level a hybrid approach is used combining old ideas of array formation and coupling applied to a novel device involving nanowire array resonators. In this study, it is first time investigated to use vertically arrayed silicon nanowires as coupled resonators for signal enhancement. In vertically arraying, nanowire resonators are placed within an array that is perpendicular to the plane of the chip. This way, the final device size becomes independent of the number of resonators used. In order to achieve this goal, mechanical coupling elements as thin membranes were designed for providing coupling between resonators. In order to demonstrate the possible outcome of this design a modeling procedure was developed for this kind of geometry. In this modeling procedure various aspects of the nanowire resonators are studied using finite element analysis (FEA) program COMSOL Multiphysics, MATLAB and finally LTspice. Equivalent circuit modeling approach is utilized for demonstration of the signal levels of single and vertically arrayed silicon nanowire (SiNW) resonators.

In Chapter 2, the need and use of mechanical coupling in array resonators in MEMS and NEMS field explained above will further be discussed. The implementation of the mechanical coupling idea to vertically stacked silicon nanowire resonators, the design and operation of the coupling membrane will also be given.

In Chapter 3, the equivalent circuit modeling based on direct (impedance) analogy and its use in flexural mode resonator will be discussed. Also, electrical equivalent circuit modeling approach of coupled array nanowire resonators will also be explained.

In Chapter 4, nanofabrication methods used to fabricate vertically stacked SiNW array resonators will be explained. The results of two test runs to fabricate vertically arrayed SiNWs will be given. A complete fabrication flow including metal electrode formation will also be provided.

In Chapter 5, the results of fabrication and modeling efforts will be summarized.

In Chapter 6, successful designs providing detectable signals will be given as a future device realization.

Chapter 2

NANOWIRE ARRAY AS A COUPLED RESONATOR

2.1 Arraying and the Coupling

In Chapter 1, all detection schemes investigated suffer from the results of extremely small sizes in NEMS resonator field. Either the small displacements create small signals or it becomes completely impossible to detect the vibration at all for the diffraction based methods. Some enhancements were proposed regarding to amplifying signal or subtracting the background by using electronic methods. Although these are useful and should be used, there is need for more intrinsic, design-based solutions in order to complete the transition from microscale devices to nanoscale. For capacitive transduction methods, there are basically three methods for decreasing the motional resistance R_m and increasing the signal. For capacitive transducers $R_m \sim \frac{d^4}{V_p^2}$, where d is electrode to resonator gap and V_p is applied dc polarization voltage[43]. So, the first two methods are based on reduction of electrode to resonator gap and increasing the dc polarization voltage. However both of them suffer from nonlinearity[42]. The third method is increasing the signal by summing the individual signals of identical resonators and arraying them. This way, the motional resistance R_m decreases almost proportional to the number of identical resonators used. The difficulty of this method is since it is very hard to fabricate exactly identical resonators at micro or nanoscale. Arraying is so sensitive to the structural differences between the resonators that may arise from fabrication, and the modes of vibrations are decoupled even for about %5 frequency mismatch (Fig. 2.1).

To overcome this problem mechanical coupling is used to generate one mode from resonators having structural differences arising from fabrication. This way, all the resonators vibrate at the same frequency generating a higher signal output. Coupled

resonators simulations show an increase in the signal level almost proportional to the number of resonators which reflects the purpose of arraying (Fig. 2.2).

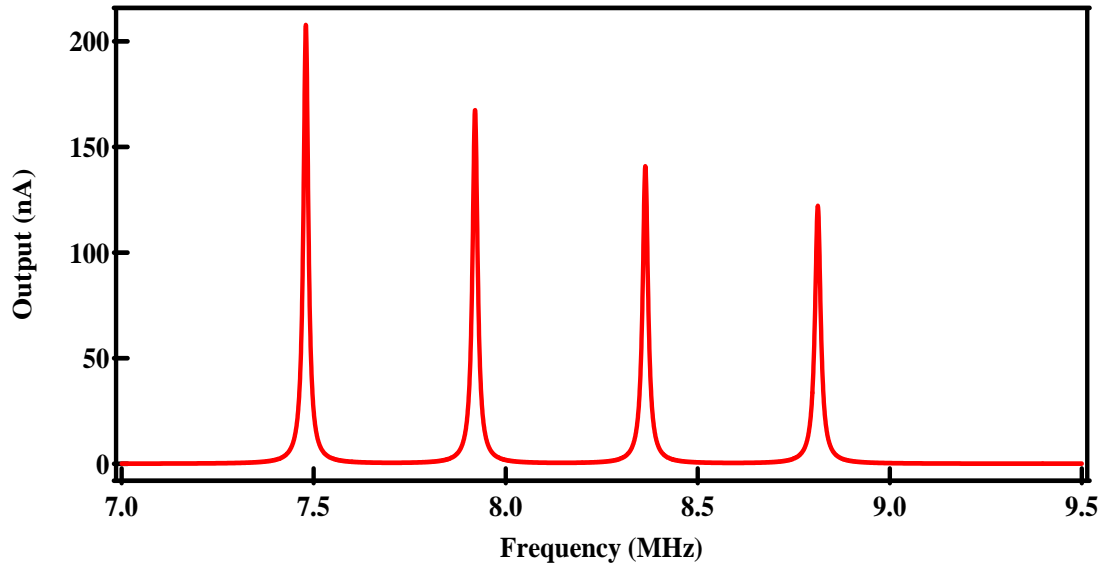


Fig. 2.1 Nanowire resonators having about 5% frequency mismatch result in decoupling.

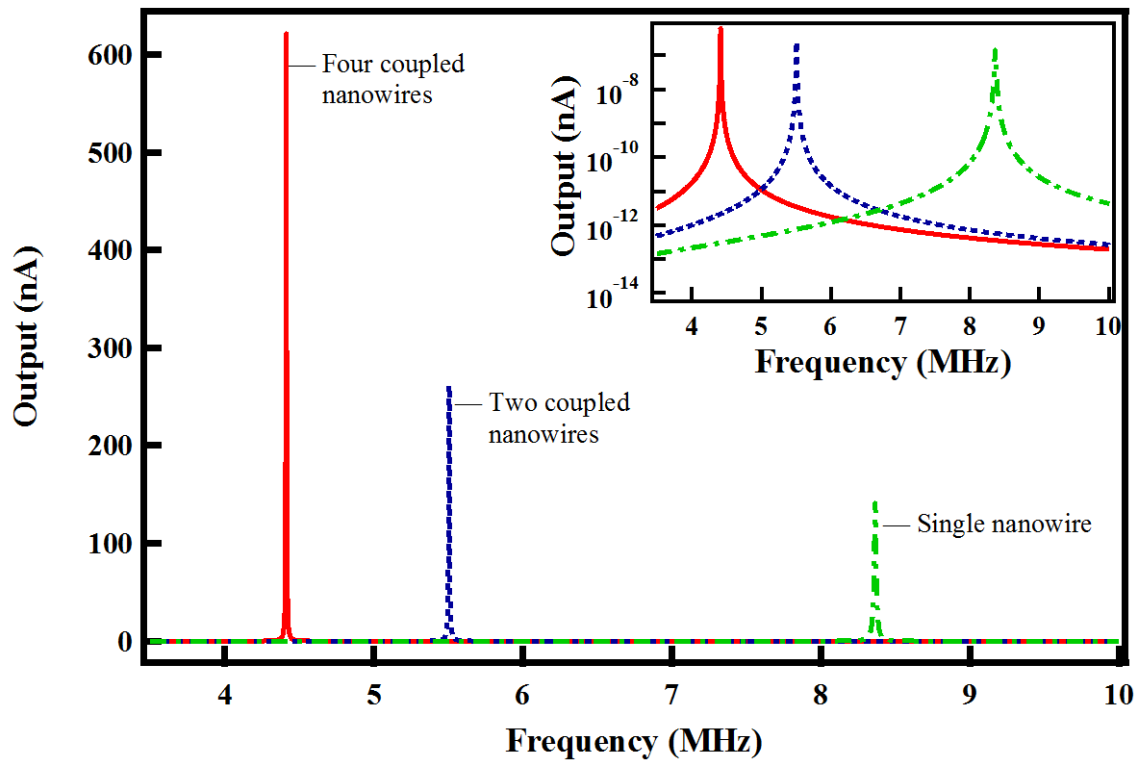


Fig. 2.2 Signal outputs of single, two coupled and four coupled nanowire resonators. Inset shows the same graph with output axis in logarithmic scale.

2.2 Micro and Nanomechanical Resonators Field with Mechanical Coupling

There are many instances utilizing above described method to increase the signal level of micro and nanoresonators. One of the first MEMS filters is realized with a comb drive architecture with three mechanically coupled resonators operating at 300 kHz with a $Q=590$ [44, 45]. The design and coupling mechanisms are studied along with equivalent circuit modeling methods with comb drive architecture until early 2000 [46]. Having similar mechanical filter design methods with previous macroscopic devices helped much to realize MEMS filters with desired characteristics. C.T.C. Nguyen and R.T. Howe patented this comb drive architecture in 2001 [47].

Filter frequencies around 8 MHz and Q factors between 40 and 450 are demonstrated in a configuration with two mechanically coupled doubly clamped beam resonators [48]. This study also utilizes the above mentioned filter design method utilizing finite element analysis (FEA) and circuit modeling (See Chapter 3 and Appendix A). Since flexural beam resonators provide higher frequencies than the comb drive transducers, beam resonators are studied in various applications: mixer-filters, coupled free-free beam resonator arrays with five, ten and twenty resonators for improved phase noise [49] and resonators with different coupling lengths and schemes for engineering the filter output signal [50]. One patent comprising coupled beam structure is filed in 2005 [51].

A rather different architecture utilizing coupled square flexural-mode microresonators is announced in 2005 [52]. In a study, seven coupled square flexural-mode microresonators are utilized at 70MHz with Q in excess of 9000 [42]. In 2006 disk array rather than square microresonators are implemented [53]. Doubly clamped and cantilever beams with various V-shaped coupling elements are studied with above mentioned conventional design methods [54]. The same lateral filter with U-shaped coupling element is demonstrated with 26 MHz operation frequency [55]. A patent is filed containing design and fabrication of coupled hollow disk resonators [56]. In another study, enhancement of Q factor by arraying of wine-glass-disk resonators is demonstrated [57]. This study offered a hybrid use of low impedance piezoelectric transducers with high Q capacitive transducers by mechanical coupling. Another patent is filed on different mechanically coupled resonator geometries such as rings with bending and breathing mode in triangle, square, hexagon shapes [58].

In 2009, it is shown that the use of mechanically coupled arrays reduces device-to-device resonance frequency variation and hence allows batch fabrication of microresonators [59].

Other current patent filings include coupled MEMS tuning forks [60] N-coupled microresonators as bandpass filters [61] and a nanosized coupling element with very low mass for MEMS filter devices in order to prevent mass loading effects [62].

2.3 Mechanical Coupling in Vertically Stacked Silicon Nanowire Resonators

Mechanical coupling became a reliable signal increasing technique and essential for operation of mechanical filters in NEMS and MEMS field. However, almost all of them were fabricated by planar processing methods and they were arrayed horizontally with respect to the substrate. Although, MEMS technology allows miniaturization and arraying over quartz resonators, the size of the resonator array increases proportional to the number of resonators implemented. However, in vertical arraying of nanoresonators, as will be explained, the size of the resonator array is independent of number of resonators. Moreover, thanks to its inborn architecture there is no need for further design and actuation of individual electrodes to obtain desired in-phase vibration mode, while suppressing the others as it is done before in the corresponding literature [42]. Vertically arraying accentuates the desired in-phase mode naturally by having single actuation electrode.

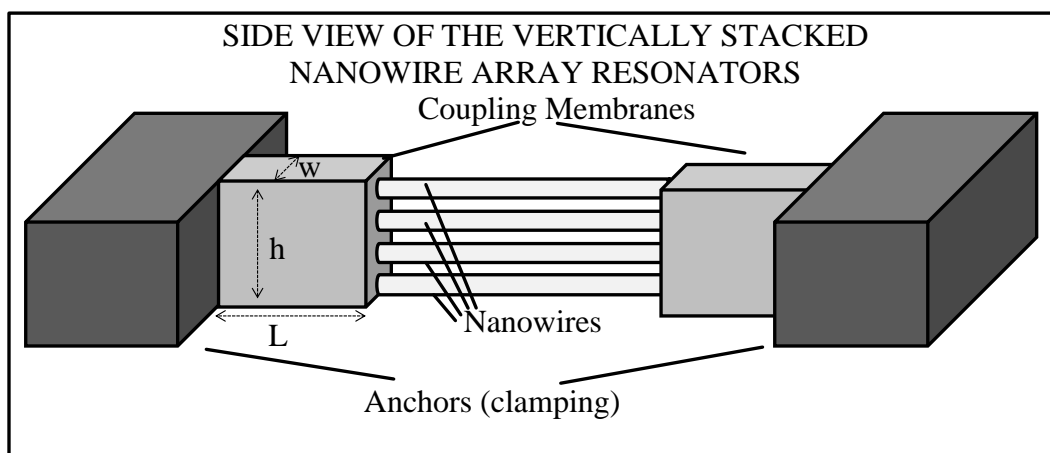


Fig. 2.3 Side view of the vertically stacked nanowire array resonators.

The mechanical coupling is obtained by thin membranes between the resonators and the anchor points. The center frequency of the composite resonator and other coupling parameters are defined by width (w), height (h) and length (L) of the coupling membrane (Fig. 2.3). Here, height stands for distance between two nanowire resonators, actually corresponds to coupling beam length. If the stiffness of the coupling membrane becomes smaller, the actuation energy dissipated into the motion of compliant spring and naturally membrane center frequency drops. Conversely, when the stiffness of the membrane increases, the nanoresonators cannot mechanically communicate through membranes and hence decoupling occurs. The membrane is designed by considering center frequencies and coupling of nanomechanical resonators. The mechanical coupling schemes explained above were simulated using COMSOL Multiphysics: Eigenfrequency module with anisotropic single crystal silicon $\langle 110 \rangle$ orientation parameters (Fig. 2.4) [63]. In COMSOL Multiphysics the X-Y drawing plane is oriented to $\langle 100 \rangle$ directions. In order to generate a simulation based on nanowires fabricated with $\langle 110 \rangle$ orientation shown in Fig. 2.4, the user needs to rotate the drawing layout by 45° . If this orientation difference in COMSOL layout and the silicon wafer taken into consideration, the resonance frequency could vary by almost 30% [63].

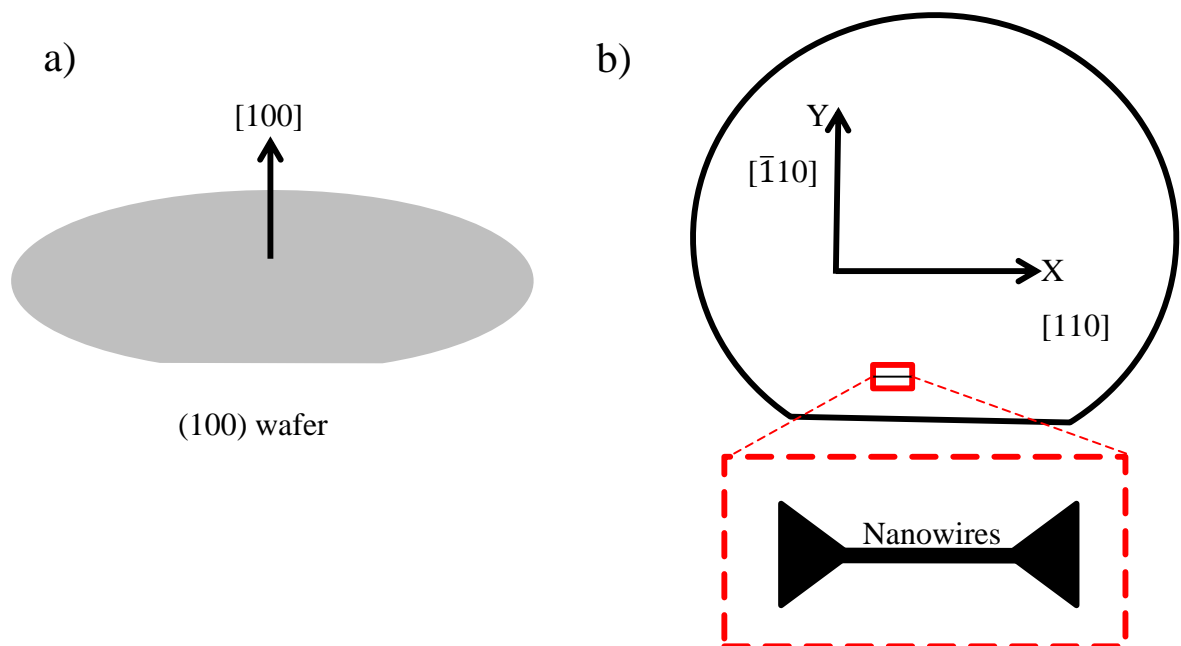


Fig. 2.4 a) Crystal orientation of a (100) silicon wafer. b) Directions and axes in a (100) wafer.

Chapter 3

COUPLED NANOWIRE ARRAY RESONATORS

In Chapter 2, the idea of vertically arraying of silicon nanowire resonators and coupling them through thin membranes at both sides were demonstrated. In this chapter, electromechanical analogies by which equivalent electrical circuit of the nanowire resonators were constructed were investigated. Finally, we will show how coupled nanowire array resonators are simulated by equivalent electrical circuit and demonstrate the enhancement in the signal level.

3.1 Electromechanical Analogies

Electromechanical components consist of mechanical elements that have influence on electrical domain. For example, loudspeakers, microphones, phonograph pick-ups, robot arms are electromechanical transducers converting mechanical energy into electrical energy and/or vice versa. The usage of equivalent circuit modeling for such electromechanical elements dates back to 1920's [64]. Different electromechanical analogies are established between electrical and mechanical domains through history. Basically, the two main methods currently used are namely direct (impedance) analogy and inverse (mobility) analogy. Both of methods have their own advantages and both of them are used quite commonly. In direct analogy, force corresponds to voltage and velocity corresponds to current (Table 3.1) and in inverse analogy, force corresponds to current and velocity corresponds to voltage. In this section direct analogy will be explained and all the relations in this thesis were constructed using direct analogy otherwise indicated.

The similarity between governing equations of mechanical and electrical energy domains allow one to express the mechanical properties of transducers by lumped electrical elements. The validity of the lumped element modeling is established by modern network theory [65]. Using electrical equivalent circuits of the electromechanical systems gives insight about the operation of the device. The existence of useful computer programs of network analysis such as SPICE (simulation program with integrated circuit emphasis)

makes this method more advantageous to understand the fully electrical response of devices which operate at different energy domains (*e.g.*, a capacitive resonator). Once the equivalent circuit is constructed one can simulate the physical behavior of the device using these computer programs.

Table 3.1 Effort-flow relations of electrical and mechanical energy domains.

General	Electrical Domain	Mechanical Domain
Effort (e)	Voltage (V)	Force (F)
Flow (f)	Current (I)	Velocity (V)
Displacement (q)	Charge (Q)	Displacement (x)
Momentum (p)	-	Momentum (p)
Resistance	Resistance (R)	Damping (b)
Capacitance	Capacitance (C)	Stiffness (k)
Inertance	Inductance (L)	Mass (m)
Node law	Kirchoff's current law (KCL)	Continuity of space
Mesh law	Kirchoff's Voltage Law (KVL)	Newton's 2 nd law

In this analogy, a spring mass system for spring constant k , mass m and damping coefficient b has force equation [7];

$$F \sin \omega t = m \frac{d\dot{x}}{dt} + k \int \dot{x} dt + b\dot{x}. \quad 3.1$$

where, \dot{x} is velocity and ω is the natural resonance frequency and $\omega = 2\pi f = \sqrt{\frac{k}{m}}$.

We know for an RLC circuit that Kirchoff's voltage law is;

$$V(t) = L \frac{di}{dt} + \frac{1}{C} \int i dt + R\dot{x} \quad 3.2$$

These equation sets in differential form are quite similar. When velocity (\dot{x}) is expressed as current (i) (*i.e.* direct analogy) mass (m) is analogous to inductance (L), stiffness (k) is analogous to inverse of capacitance (C) and damping coefficient (b) is analogous to resistance (R) (Fig 3.1). Sometimes these RLC values are called as motional inductance L_m , motional capacitance C_m and motional resistance R_m .

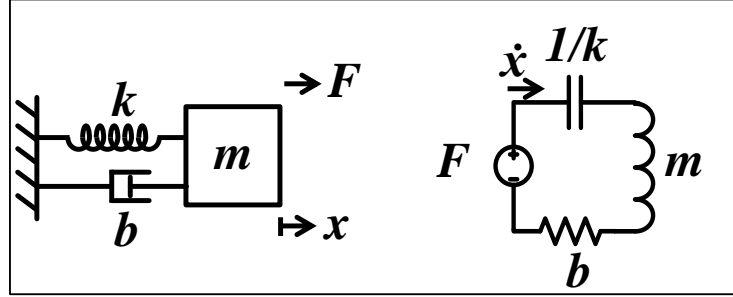


Fig 3.1 Equivalent RLC circuit of the lumped mass stiffness damper model in direct analogy.

The full relation between mechanical and electrical sets are obtained by an electromechanical transduction factor, η . Since there is an analogy between force and voltage and velocity and current one can write relationships;

$$V = F \cdot \epsilon_F, i = \dot{x} l_v \quad 3.3, 3.4$$

where ϵ_F and l_v are force and velocity scale factors. ϵ_F corresponds to $\frac{\text{voltage}}{\text{force}}$ and l_v corresponds to $\frac{\text{current}}{\text{velocity}}$ [66].

And by definition mechanical impedance, Z_m is

$$Z_m = \frac{F}{\dot{x}} \quad 3.5$$

Rewriting electrical impedance using Equations 3.3, 3.4 and 3.5 we will obtain

$$Z_e = \frac{V}{i} = \frac{F \cdot \epsilon_F}{\dot{x} l_v} = Z_m = \frac{Z_m}{\eta^2} \quad 3.6$$

where, $\eta^2 = \frac{l_v}{\epsilon_F}$ [66]. This way, the full relationships between mechanical and electrical relations are given;

$$R = \frac{b}{\eta^2}, L = \frac{m}{\eta^2}, C = \frac{\eta^2}{k} \quad 3.7$$

Electromechanical transduction factor, η , changes due to the type of vibration of the mechanical part (e.g., bending mode vibration clamped-clamped beam and wine glass mode vibration of disks) and the electrical detection method utilized and hence the governing equations change. The equivalent circuit calculation of bending mode clamped-clamped beam [48] and MATLAB code related to this calculation is given in Appendix A.

In this approach clamped-clamped silicon nanowire resonators are modeled as bending mode clamped-clamped beam.

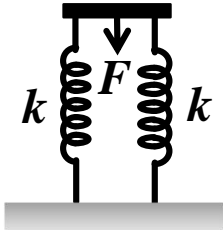



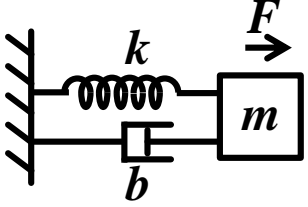
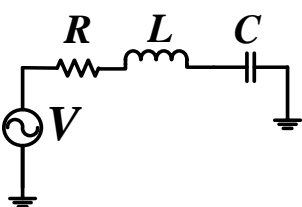
After having converted lumped parameters of the resonator to the electrical domain, they should be connected to each other correctly. In direct analogy, simple rule of thumb is when two mechanical elements' impedances add, they are said to be parallel and if admittances add they are called series. And when converting these connections the rule is;

Mechanical parallel connection \longleftrightarrow Electrical series connection

Mechanical series connection \longleftrightarrow Electrical parallel connection

However, the connection of masses needs a more careful approach. The masses appear to be series combination at first glance is called parallel in this analogy [66]. Please see Table 3.2 for the examples and explanations of these connection rules.

Table 3.2 Connection rules for mechanical and electrical networks.

MECHANICAL	ELECTRICAL
 <p>Impedances add \rightarrow Parallel</p>	 <p>Impedances add \rightarrow Series</p>
 <p>Impedances add \rightarrow Parallel</p>	 <p>Impedances add \rightarrow Series</p>
	

3.2 Equivalent Circuit Model of Single Nanowire Resonator.

A basic excitation layout for single nanowire resonator and its equivalent circuit is given in Fig 3.2. 50Ω resistances and parasitic capacitance (C_p) are stemmed from input and output cabling. Electrode to resonator capacitance C_0 was also included in the equivalent circuit. Most importantly electrode to electrode feed through capacitance C_F is

parallel to the resonator and for this reason it is parallel to the RLC in the equivalent circuit.

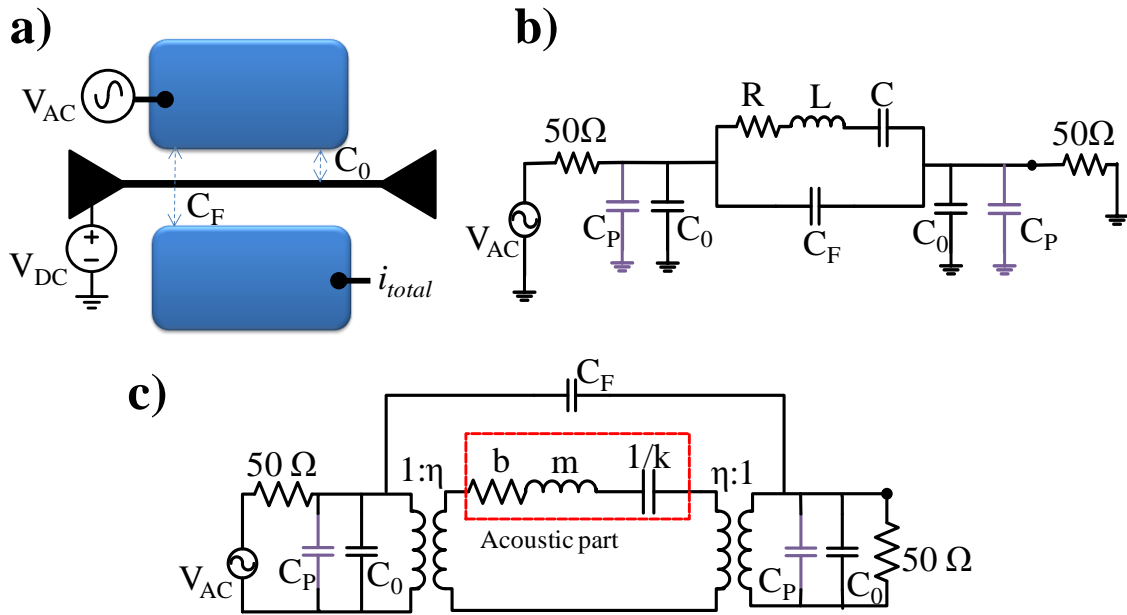


Fig 3.2 a) Top view of the nanowire resonator layout including ac and dc voltages and read out nodes. b) Electrical equivalent circuit of this layout with input/output capacitances and resistances which are typically 50Ω . c) Electrical equivalent circuit of the same with transformer model.

In Fig 3.2.a) top view of the resonator device is shown and in Fig 3.2. b) its all-electrical equivalent circuit is shown. Sometimes the equivalent electrical circuit is constructed with transformers (Fig 3.2.c)). This way, the circuit elements between two transformers are said to be in mechanical domain. Transformer turns ratio is used as electromechanical transduction factor. The circuit in Fig 3.2.a) and Fig 3.2.b) give basically the same results.

The values of RLC is calculated from the layout parameters such as electrode to resonator gap (d), dc bias (polarization) voltage V_{DC} , length (L), width (w) and height (h) of the nanowire. Parasitic capacitance (C_P) due to cabling is measured as a few hundreds of femtofarads in general for 50Ω coaxial cables and the values of feed through capacitance (C_F) and electrode to resonator capacitance (C_0) is calculated using Electrostatic Module of COMSOL Multiphysics for the given layout parameters. (Appendix B)

For a single resonator with parameters given in Table 3.3, the simulated signal output of Design 1 is shown in Fig 3.3. The first peak corresponds to the resonator RLC and the second is due to the parallel capacitance. The magnitude measured is 0.33dB which is challenging to detect or name as a resonance peak under measurement setup. It is because the feed through capacitance dramatically reduces the signal level. Keeping the same resonator and reducing the electrode to resonator gap, d and thus reducing the bias voltage to prevent pull-in, Design 2 parameters obtained to enhance the result. Although, ten times smaller Q factor is proposed, Design 2 gives 15.9dB signal which makes it a quite acceptable design in terms of detection (Fig 3.4). A simple optimization in the electrode to resonator gap resulted considerable difference in read out signal and hence should be studied during design process.

Table 3.3 Silicon nanowire resonator design and parameter summary.

Parameter	Design 1	Design 2	Unit
Length of the resonator, L	10	10	μm
Width of the resonator, W	100	100	nm
Height of the resonator, h	100	100	nm
Electrode to resonator gap, d	450	250	nm
DC bias, V_{DC}	40	25	V
Quality factor, Q	5000	500	-
Electrode width, W_e	10	10	μm
Gate capacitance, C_g^*	0.21	0.26	fF
Feedthrough capacitance, C_F^*	300	300	fF
R^{**}	819	0.992	$\text{k}\Omega$
L^{**}	74.1265	0.0897	H
C^{**}	0.00441	3.65	fF

**Calculated using FEA program (See Appendix B).*

*** Calculated from the formulation and code given in Appendix A*

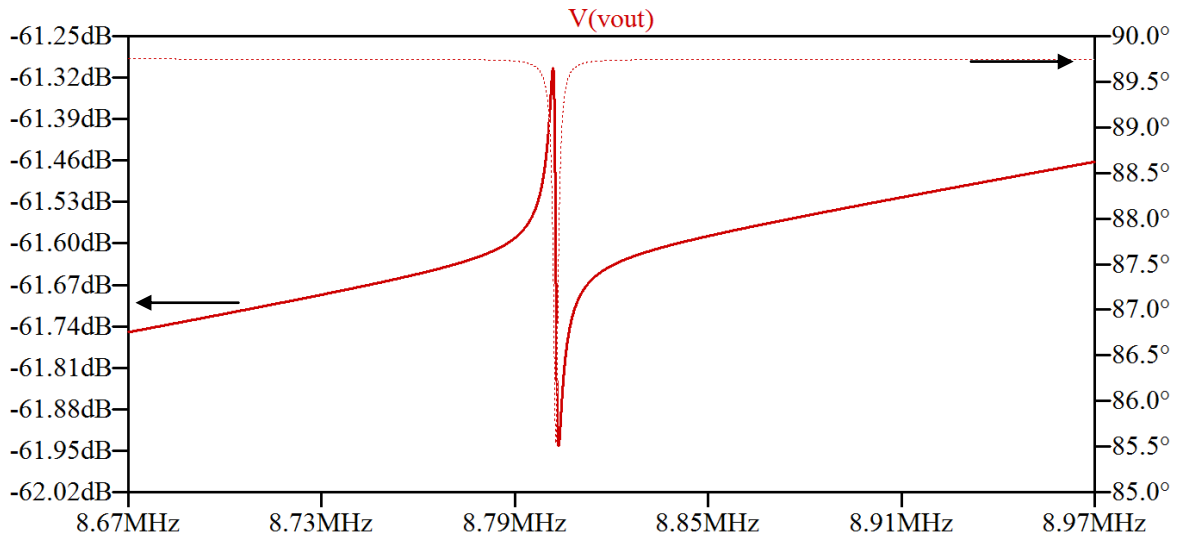


Fig 3.3 SPICE equivalent circuit model result of Design 1.

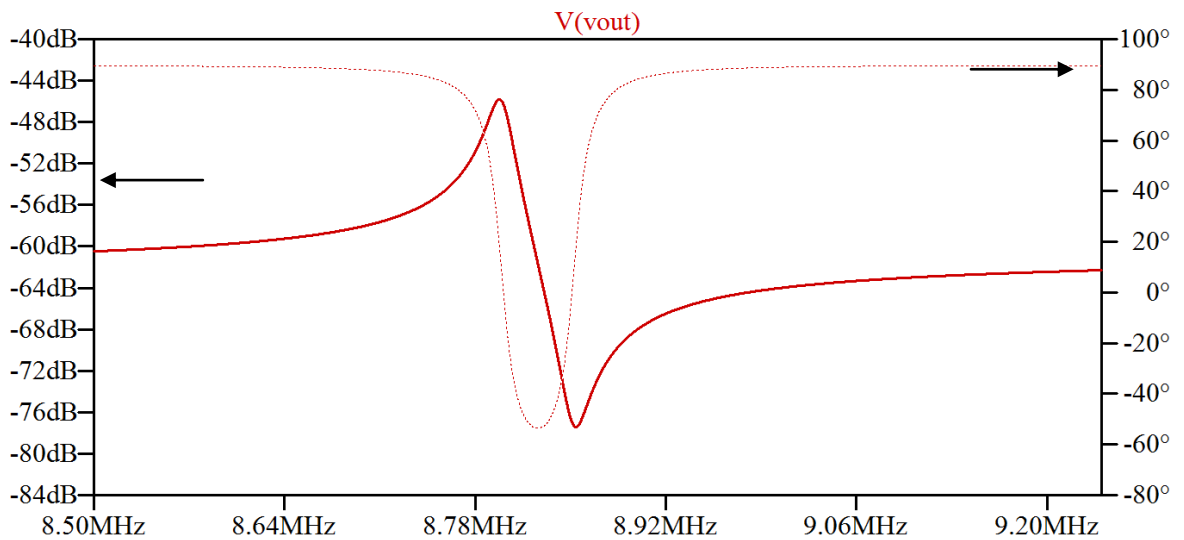


Fig 3.4 SPICE equivalent circuit model result of Design 2.

3.3 Equivalent Circuit Modeling of Coupled Array resonators

Equivalent circuit modeling of the coupled array resonators is achieved by using the same formulation explained in previous sections with an additional procedure for mechanical coupling. After obtaining equivalent RLC results of the individual resonators, coupling membrane of the array resonator is designed using Structural Mechanics module of COMSOL Multiphysics to obtain the desired coupling scheme. Having designed the coupling membrane width and length, eigenfrequencies of the four modes are determined using the same simulation (Fig 3.5).

The frequencies of the each mode of vibration are used as template for determining the electrical equivalents of coupling membranes to set resonant modes to these frequencies (Fig 3.6). Equivalent circuit of the array resonators is drawn using the RLC values of the four resonators, estimated C_P , C_F and C_0 values and LC values corresponding to coupling. The coupling structures modeled as T-networks using inductors and a capacitor in Fig 3.8. The inductance corresponds to mass and capacitance corresponds to stiffness of the coupling membranes. LC values of the coupler are determined by matching the COMSOL simulated frequencies. This method is utilized in MEMS literature for determining LC values of the coupling structure [42]. When frequencies of the four modes are fitted to the mode frequencies obtained by COMSOL, the effect of coupling structures on the whole structure is successfully transferred to the electrical equivalent circuits.

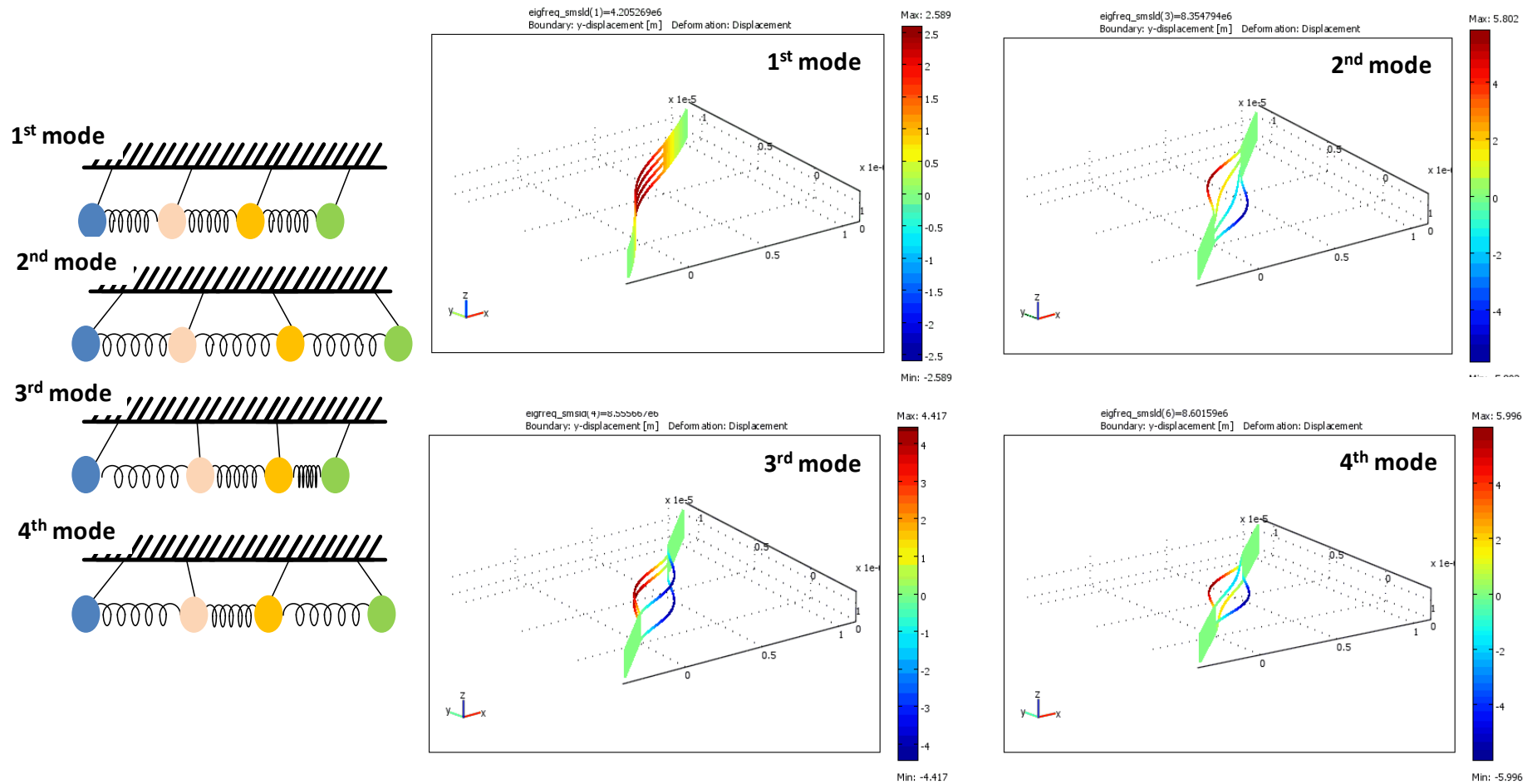


Fig 3.5 Four mode shapes and eigenfrequencies of coupled array resonators demonstrated by COMSOL Multiphysics.

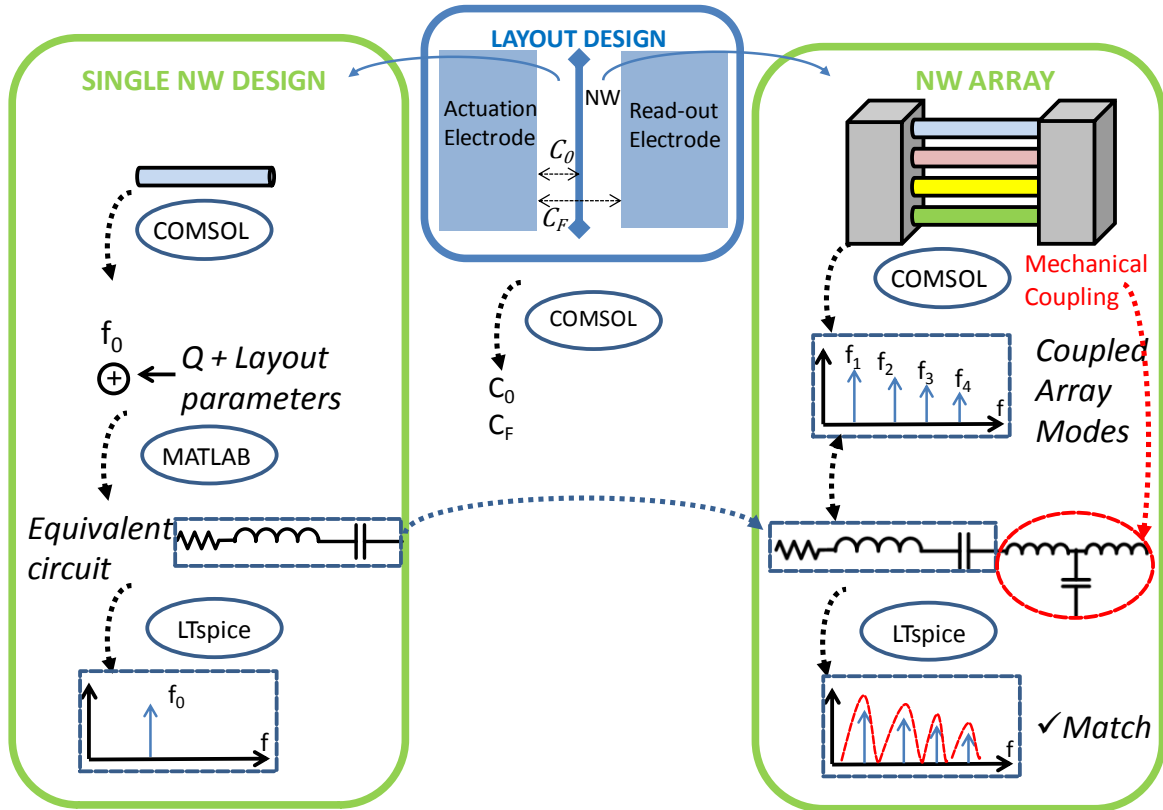


Fig 3.6 Summary of the modeling procedure for single and coupled array nanowire resonators.

SPICE circuit drawn for the scenario of an array of resonators, which have 5% frequency deviation due to fabrication imperfection is seen in Fig 3.8. Transformer turns ratios were all normalized to 1:1 for ease of calculation and the RLC values of electrical domain given in Eqn. 3.8 were calculated and used for this circuit. Four resonance peaks were fitted to the COMSOL simulated frequencies by changing L and C values of the coupling part in the circuit (Fig 3.8). Signal of the first peak is shown in Fig 3.7. This resulted a 2.76 dB signal, which is high enough to discriminate it as a sign of resonance. Previously, single nanowire resonator was shown to have a signal of 0.637dB for the parameters of NW1 of Table 3.4, which is not sufficient for determining a resonant peak. The result shows the success of the coupled arraying method.

Table 3.4 Nanowire resonator parameter summary for coupled array simulations.

Parameter	NW 1	NW 2	NW 3	NW4	Unit
Length of the resonator, L	10	10	10	10	μm
Width of the resonator, W	100	95	90	85	nm
Height of the resonator, h	100	95	90	85	nm
Electrode to resonator gap, d	450	450	450	450	nm
DC bias, V_{DC}	40	40	40	40	V
Quality factor, Q	5000	5000	5000	5000	-
Electrode width, W_e	10	10	10	10	μm
R^*	0.819	0.71	0.597	0.481	$\text{M}\Omega$
L^*	74.1265	67.56	60	51.16	H
C^*	0.00441	0.0054	0.0067	0.00885	fF

* Calculated from the formulation and code given in Appendix A.

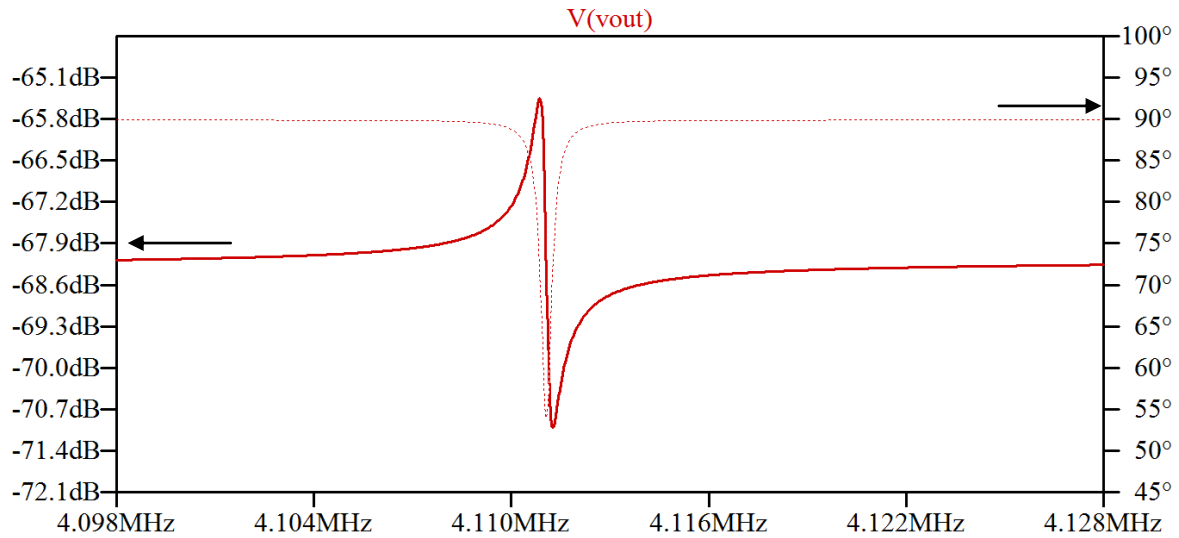


Fig 3.7 SPICE equivalent circuit model result of array resonators.

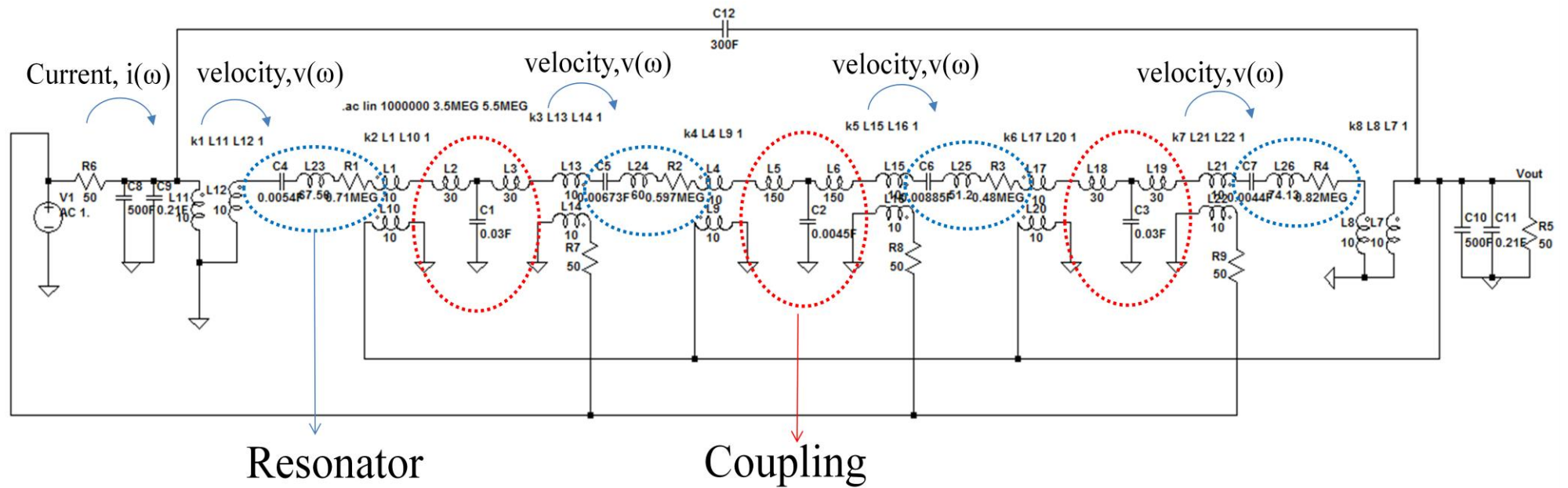


Fig 3.8 SPICE circuit equivalent for four coupled nanowire resonators geometries of which are given in Table 3.4.

Chapter 4

FABRICATION

In this chapter, the fabrication process of the vertically stacked silicon nanowire array will be explained. Fabrication of a vertically stacked silicon nanowire array was aimed by utilizing the Bosch process [67]. The fabrication test runs were completed by Berkay Gümüş during his visit to clean room facilities at Center of Micronanotechnology (CMi), Swiss Federal Institute of Technology (EPFL) in January and February, 2012. In the two test runs the maximum nanowire lengths were characterized for a certain recipe. In the first run, nanowires having lengths ranging from $2\mu\text{m}$ to $30\mu\text{m}$ were fabricated. Although we achieved vertical stacking, adhesion of some of the nanowires to one another was realized. In a second test run, nanowire arrays with lengths ranging from 500nm to $1.8\mu\text{m}$ were fabricated successfully without having previous adhesion problem. Moreover, a complete fabrication flow including electrode formation is also proposed in this chapter.

4.1 Process Flow

Process flow for the nanowire resonators on a silicon wafer is shown in Fig. 4.1. In the first test run, nanowire lengths ranging from $2\mu\text{m}$ to $30\mu\text{m}$ were characterized. Firstly, HSQ e-beam resist is patterned with varying widths from 50nm to 100nm using Vistec EBPG5000. The aim for this is to observe the transition from membrane to vertically disconnected nanowires. Then, Bosch process is applied to obtain nanowires from two neighbor trenches that are close enough to facilitate meeting of etch scallops from both sides along the centerline of the dividing mask. Etching was carried out using Alcatel AMS 200 DSE with a recipe called ZZ_SOI_accu2 given in Table 4.1. The optimum etching time was determined as 22 seconds. This etching time is enough to reach buried oxide layer (BOX) of silicon on insulator (SOI) wafer with 340nm -thick device layer. This way, the nanowires were isolated *i.e.*, adjacent nanowires being disconnected from each other. Finally e-beam resist is removed by HF vapor using IDONOUS HF-VPE 100. The removal time is around 3 minutes. HF vapor process rather than wet processes is preferred to avoid adhesion.

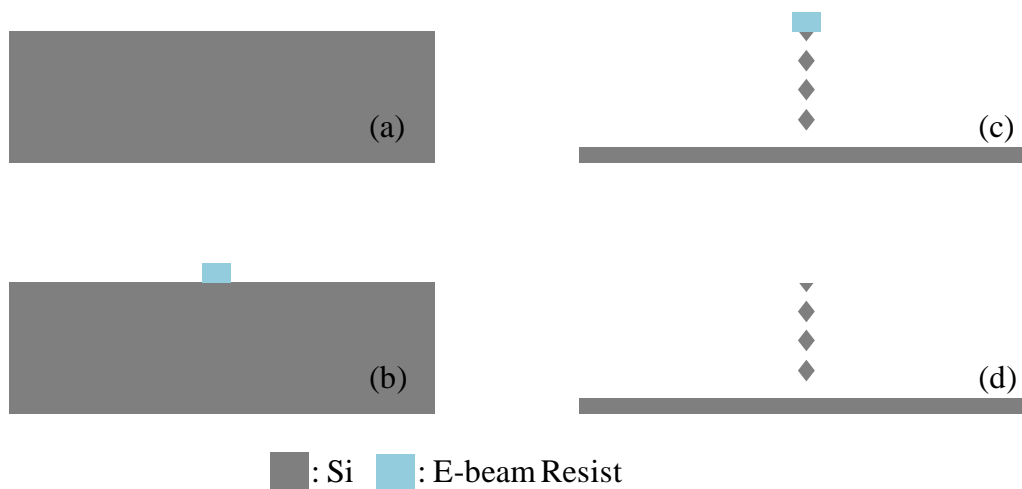


Fig. 4.1 Process flow for the fabrication of silicon nanowire array (a) wafer preparation, (b) e-beam lithography, (c) Bosch process, (d) HF vapor e-beam resist removal.

First run that characterizes nanowire lengths varying from $2\mu\text{m}$ to $30\mu\text{m}$ ended up with an adhesion problem as can be observed in Fig. 4.2. In Fig. 4.2, two nanowires on the top and two nanowires at the bottom have adhesion at the mid section for a $2.5\mu\text{m}$ -long nanowire array although individual resonators can be seen near anchor points. The fifth line is occurred in fourth cycle of the Bosch process and did not form an isolated nanowire structure. For longer nanowire sets the adhesion was more severe and hence it is decided to fabricate nanowire arrays shorter than $2\mu\text{m}$ for this recipe.

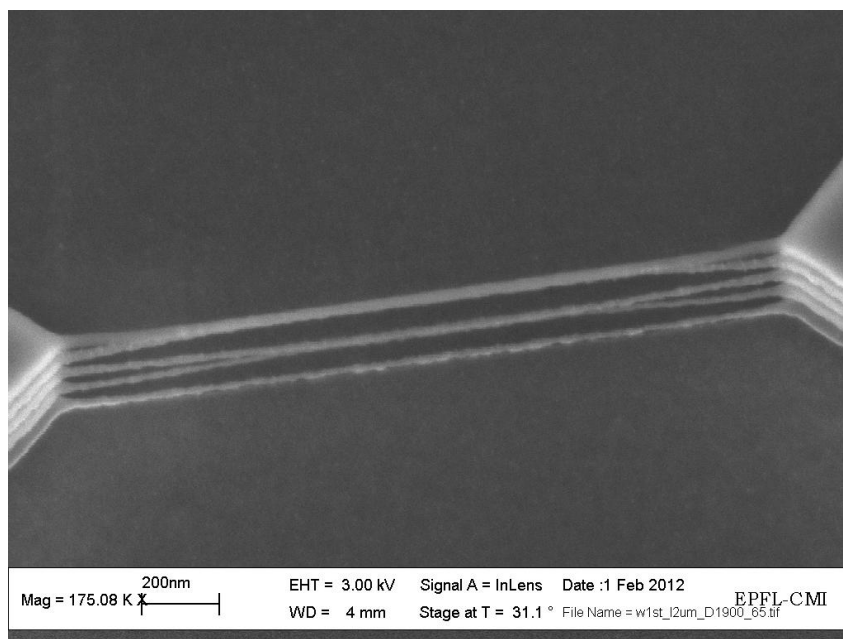


Fig. 4.2 A $2.5\mu\text{m}$ -long nanowire array SEM image.

Table 4.1 The recipe of Bosch process ZZ_SOI_accu2 for nanowire fabrication.

SF₆ Flow	100sccm
SF₆ Time	2.8s
C₄F₈ flow	75sccm
C₄F₈ time	1.5s

In the second run, the nanowire lengths were varying between 500nm to 1.8 μ m. This run resulted better and the nanowires were isolated and straight. This run was much more successful with the same recipe for both the smallest and longest nanowire arrays due to having a shorter aspect ratio. In Fig.4.3 SEM image of 1.8 μ m long nanowire array is taken after step (c) before removing e-beam resist and hence having a thicker top nanowire with respect to the substrate. The nanowire array field emission SEM image seen in Fig.4.4 is taken right after the e-beam resist removal. The successful nanowire formation is observed for 500nm-long array. Although a thin layer of HSQ e-beam resist is still observed, it has little contribution for having a larger diameter top nanowire. It is an inherent result of the Bosch process *i.e.* top nanowire has less etch surface under the mask and having effected by only two “scallops”. However, following nanowires are affected by four “scallops”, having a larger etch surface and hence a smaller diameter. (Fig.4.3)

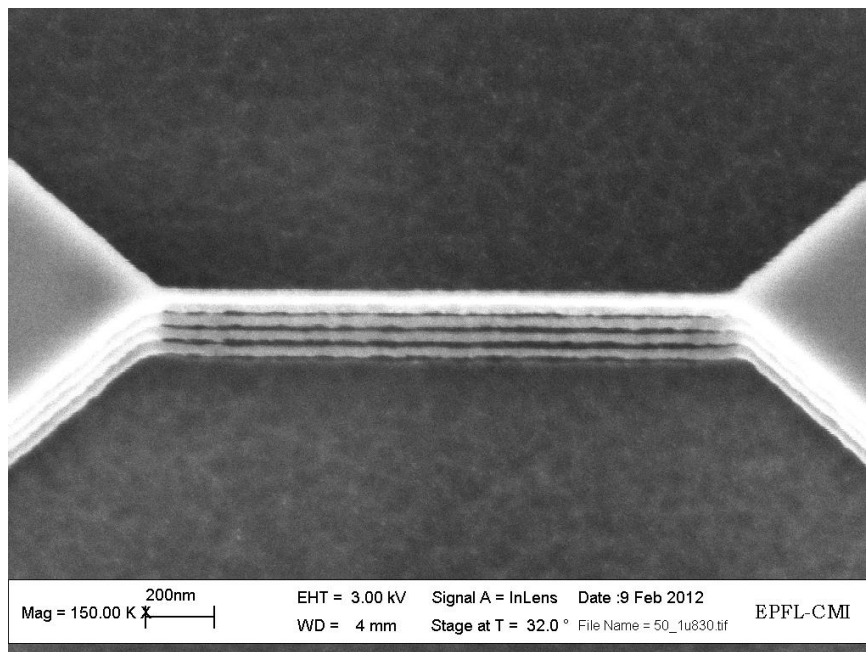


Fig.4.3 A 1.8 μ m-long nanowire array SEM image before e-beam resist removal.

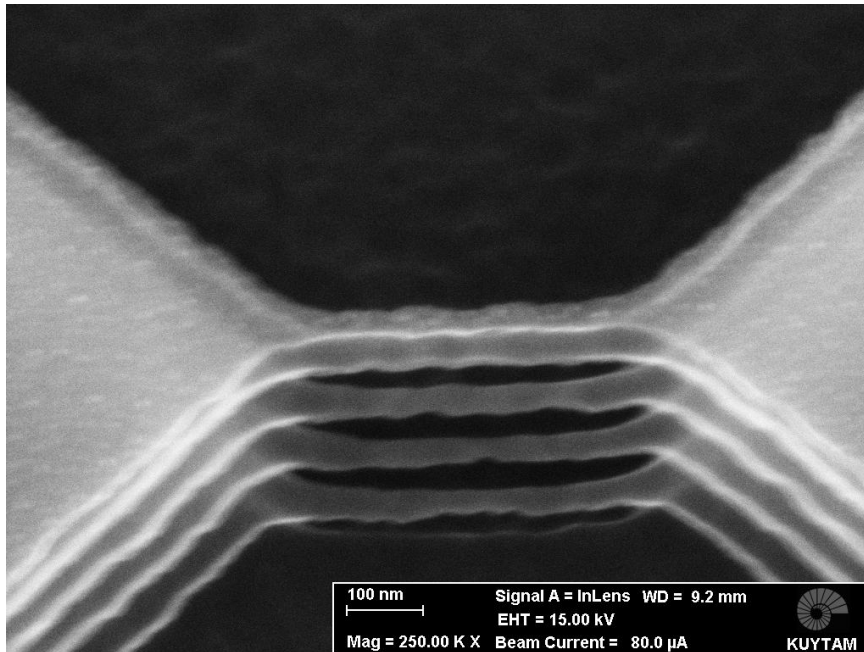


Fig.4.4 500nm-long silicon nanowire array field emission SEM image after e-beam resist removal.

4.2 Proposed fabrication flow

In order to obtain a fully operational resonator array, one needs to fabricate metal electrodes near nanowires in order to actuate and detect the vibrations of nanowires. A process flow is proposed in Fig.4.5 to achieve metal electrode fabrication along with silicon nanowire array resonators.

In this process flow a SOI wafer with a 340nm-thick device layer is used. In step (b), a 100nm thick SiO₂ layer is coated by employing dry oxidation process using Centrotherm furnaces. In step (c), negative e-beam resist of HSQ is patterned using Vistec EBPG5000. Then, oxide is etched using Alcatel AMS 200 DSE. In step (e), a photolithography process is used to define the electrode area. The photoresist (PR) AZ92XX series is coated using Ritetrack 88 Series Automatic Coater. Then, patterning of this PR was made using Süss MA150 Double Side Mask Aligner. In Fig.4.5(f), the Bosch process is applied using Alcatel AMS 200 DSE with a recipe called ZZ_SOI_accu2 given in Table 4.1. The oxide is plasma-etched using Alcatel AMS 200 DSE for 100 nm thickness. This step is necessary for avoiding the level mismatch between the nanowires and the electrodes in further steps. In Fig.4.5(g), low temperature oxide is deposited to protect the nanowires in oxide

envelope using Centrotherm furnaces. The minimum thickness of this oxide layer should be the half of the internanowire distance to avoid short contact between actuation electrode and read-out electrode. Moreover, this thickness determines the electrode to resonator gap. In Fig.4.5(h), a 340nm thick aluminum layer is sputtered to fill the electrode gaps defined in step (f). In Fig.4.5(i), an e-beam resist is spin-coated to have a planar e-beam resist surface by Ritetrack 88 Series Automatic Coater. The thickness of the e-beam resist is characterized to obtain a planar surface. In Fig.4.5(j), HSQ is etched back by Alcatel AMS 200DSE. The etching process should also be characterized to avoid etching the HSQ that protects aluminum electrodes from the previous etch step. In Fig.4.5(k), aluminum is etched using STS Multiplex ICP plasma etcher for better control over etching. This step should be controlled to avoid etching of electrode material. In step (l), chip scribing process takes place. This step should be done before release of nanowires to protect the resonating parts from physical damages. In Fig.4.5(m), the remaining e-beam resist is removed in UFT resist stripping wet bench. In Fig.4.5(n), nanowires are released by using silox bath in Plade oxide wet bench. In Fig.4.5(o), supercritical CO₂ treatment is applied to avoid adhesion using Tousimis Autosamdri 915B.

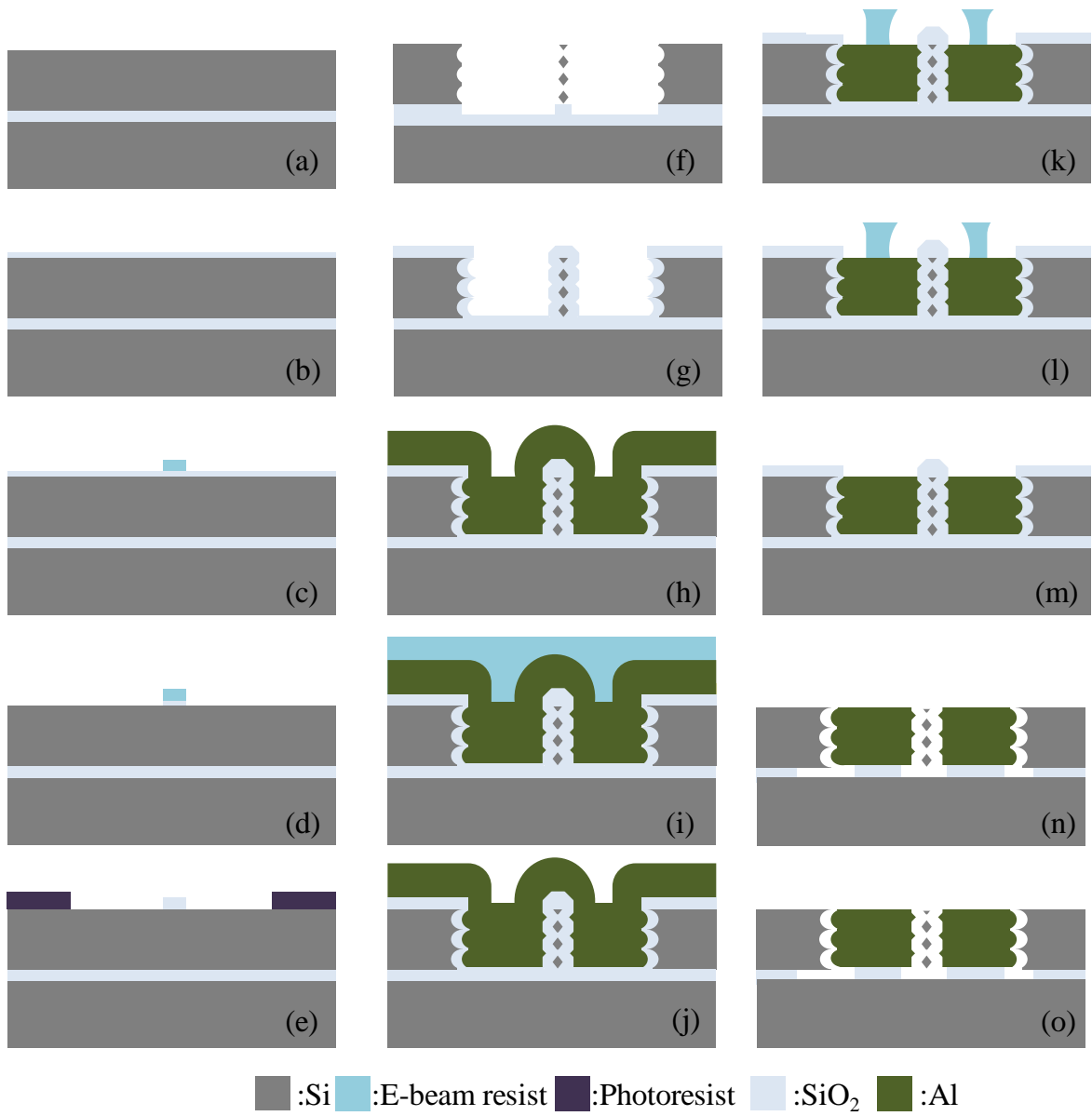


Fig.4.5 Proposed process flow for silicon nanowire resonators with metal electrodes.

Chapter 5

CONCLUSION

A capacitive transduction scheme was proposed to simplify future integration with a transistor circuit. However, the common problem for nanoscale resonators is low read out signal due to small vibration amplitudes and hence large motional resistance, R_m . In order to increase the readout signal, the idea of arraying with mechanical coupling is utilized. A novel mechanical coupling scheme was proposed for vertically stacked silicon nanowire array resonators. In this scheme, the design of coupling membrane is carried out by adjusting length and width. The height of the coupling membrane was set by the number of nanowires used

The usage of individual nanowire resonators connected to thin membranes rather than a single membrane resonator provides different frequencies needed for mixer and filter applications. A frequency mixer is a circuit that generates new frequencies from the signals applied to it and a filter removes the undesired frequency components from the signal. In order to provide these kinds of operations, non-identical resonance frequencies are needed to generate new frequencies or to set the bandwidth of the filter. For this reason, the arraying is also necessary for such application fields in which generation of different individual frequencies are needed.

An electromechanical modeling procedure for single and coupled array nanowire resonators was also developed for coupled silicon nanowire array resonators to demonstrate the possible signal level of a certain design of resonator device. The models of coupled array resonators showed substantial increase in the signal level due to addition of signals of individual resonators. This kind of equivalent circuit modeling provided insight about the operation of the devices.

Using the developed modeling tool the effect of geometrical parameters on read out signal was also demonstrated. Among these parameters feed through capacitance, electrode to resonator gap, and bias voltage have critical influence on the read out signal. Capacitances between electrodes, probes and pads contribute to the feed through capacitance, C_F . Since the latter two have capacitance on the order of hundreds of

femtofarads, whereas the electrode to electrode capacitance is on the order of few femtofarads, the reduction of C_F based on layout design is limited.

An enhancement in reduction of the C_F could be achieved by wirebonding or using ground-signal-ground (GSG)-type pads should also reduce the noise level. The usage of GSG-type pads probes and wirebonds will decrease the field coupling of the two electrodes. The electric fields emanating from signal pad will couple to the ground pad nearby and hence the C_F will reduce. Moreover, increasing the distance between electrodes will also enhance the reduction of feedthrough capacitances.

Furthermore, electrode to resonator gap should be minimized to enhance the signal level. Previously, it is stated that motional resistance is proportional to fourth power of electrode to resonator gap and inverse square of bias voltage ($R_m \sim \frac{d^4}{V_p^2}$) [43]. For this reason, adjustment of these parameters contributes most to the signal level. The lower limit of electrode to resonator gap for the Bosch process-based fabrication of silicon nanowire array resonators are determined to be the half of the vertical distance between neighbor nanowires. Oxide envelopes of adjacent nanowires should touch each other to prevent short circuit between actuation and read out electrodes. For the fabricated nanowire arrays, this distance was about 70nm for the 340nm-etched wafers. Although about 35nm of oxide deposition suffices to fill the vertical gap between nanowires and isolate two electrodes from each other, a minimum oxide of 50nm was proposed. Hence, minimum electrode to resonator gap for our previously developed recipe is defined as 50nm. Bias voltage was also maximized to reduce motional resistance without causing pull-in for designs of resonator devices.

Having learned the geometrical limitations due to fabrication constraints and the principles gained from the modeling, some realistic scenarios were investigated in Chapter 6. This way, the possible signal levels of the devices fabricated in the future is investigated.

Chapter 6

OUTLOOK

In this chapter, some possible device geometries are investigated for read out success with the fabrication output explained in Chapter 4. This way, it is aimed to proceed with resonator fabrication including metal electrodes using these layout designs. Nanowire arrays with lengths of minimum 500nm and maximum 1.8 μ m were fabricated. In these arrays, nanowire diameters increasing from the bottom to the top was observed. This difference would result in different resonance frequencies and the decoupling of the modes, if mechanical coupling is not facilitated.

In this chapter, all the nanowire resonator array sets were modeled using the procedure explained in Chapter 3. In this procedure equivalent RLC values of each nanowire resonators were calculated using the formulation and MATLAB code given in Appendix A. Mechanical coupling with membranes at both ends was modeled using Structural Mechanics module of COMSOL Multiphysics (See Appendix B).

Parasitic capacitance (C_P) due to cabling is measured as a few hundreds of femtofarads in general for 50 Ω coaxial cables and input as 500fF for all models. Capacitances between electrodes, pads and probes contribute to feed through capacitance (C_F) and are estimated to be about 300fF in total (See Appendix B) for all the cases in this chapter.

For ambient test conditions with similar characterization setup and similar devices fabricated with the Bosch process, the quality factor is reported to be 75 [24]. Since Q factor is an empirical parameter, $Q=75$ was assumed to reflect the same ambient test conditions to achieve realistic simulation results.

1.8 μ m-long nanowire array resonator parameters are summarized in Table 6.1. The circuit constructed for coupled array resonators in Chapter 3 is used for modeling (Fig 3.8). The signal output of 1.8 μ m-long nanowire array resonators is given in Fig.6.1. The signal measured is 1.8dB. In order to safely determine the resonance peak, a better quality factor needed. A $Q=150$ suffices to increase signal level by having measurements under vacuum, if better quality factor was not observed. The signal measured with $Q=150$ is 3.27dB which is sufficient to demonstrate a resonant behavior. Although single nanowire resonators have

a resonance frequency of about 50 MHz, the frequency of the first mode of vibration is 33.7MHz.

Table 6.1 Nanowire resonator parameter summary for 1.8 μm -long nanowire array simulations.

Parameter	NW 1	NW 2	NW 3	NW4	Unit
Length of the resonator, L	1.8	1.8	1.8	1.8	μm
Width of the resonator, W	28	26	24	22	nm
Height of the resonator, h	28	26	24	22	nm
Electrode to resonator gap, d	50	50	50	50	nm
DC bias, V_{DC}	9	9	9	9	V
Quality factor, Q	75	75	75	75	-
Electrode width, W_e	1.8	1.8	1.8	1.8	μm
R^*	2.1434	1.0933	0.2130	0.00572	M Ω
L^*	0.4061	0.2212	0.0471	0.0014	H
C^*	0.015715	0.0329	0.18452	7.4191	fF

* Calculated from the formulation and code given in Appendix A

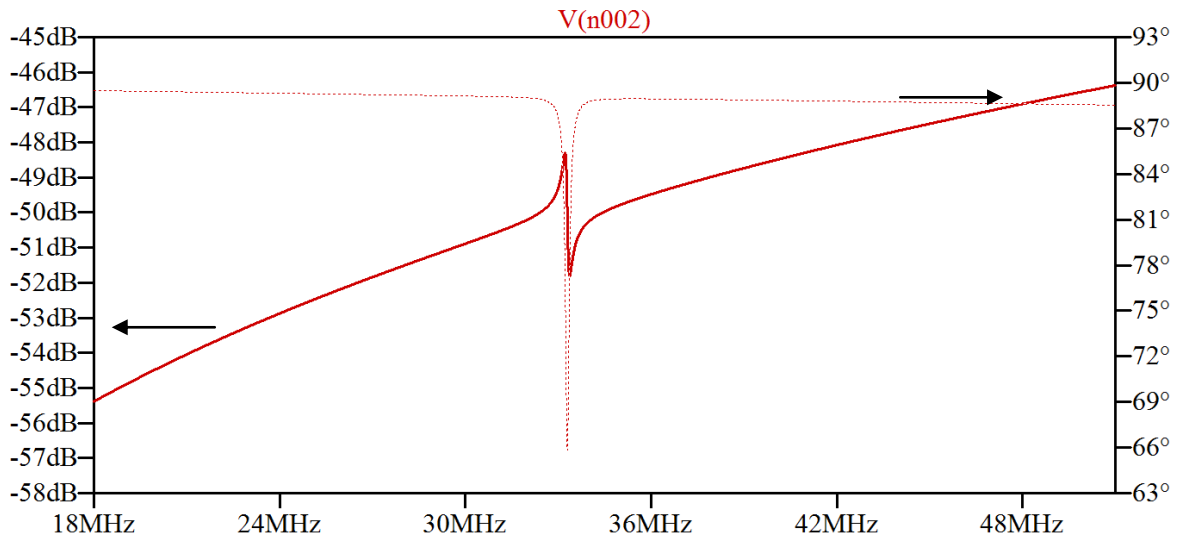


Fig.6.1 SPICE equivalent circuit model signal output of 1.8 μm -long nanowire array resonators.

For smaller lengths of nanowire arrays the signal reduces drastically, making it impossible to detect. For example, for a 1.5 μm -long nanowire array, parameters of which is given in Table 6.2 the signal output is about 0.010dB which makes it impossible to name

as a resonance. For quality factors as much as 7500 which is possible under vacuum, the amplitude of the resonance signal becomes 2.74dB (Fig.6.2).

Table 6.2 Nanowire resonator parameter summary for 1.5 μm -long nanowire array simulations.

Parameter	NW 1	NW 2	NW 3	NW4	Unit
Length of the resonator, L	1.5	1.5	1.5	1.5	μm
Width of the resonator, W	28	26	24	22	nm
Height of the resonator, h	28	26	24	22	nm
Electrode to resonator gap, d	50	50	50	50	nm
DC bias, V_{DC}	10	10	10	10	V
Quality factor, Q	75	75	75	75	-
Electrode width, W_e	1.5	1.5	1.5	1.5	μm
R^*	6.631	4.883	2.956	1.243	$\text{M}\Omega$
L^*	0.8699	0.6857	0.4524	0.2089	H
C^*	0.003517	0.0051126	0.0092033	0.024048	fF

* Calculated from the formulation and code given in Appendix A

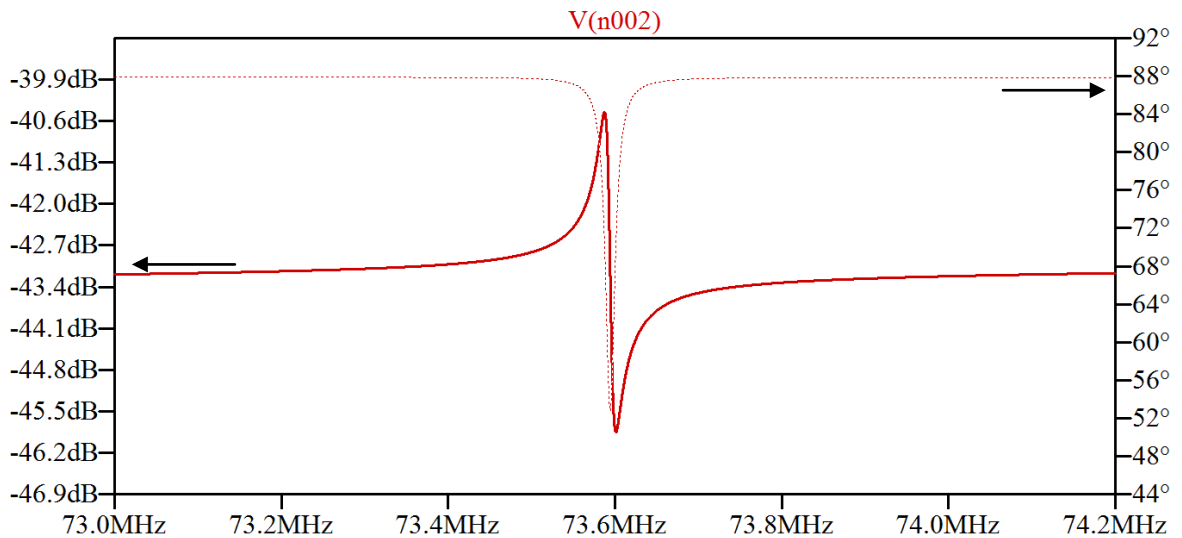


Fig.6.2 SPICE equivalent circuit model signal output of 1.5 μm -long nanowire array resonators with $Q=7500$.

Similarly, 1 μm -long nanowire array resonators (Table 6.3) have a simulation result that reflects a curve that resonance peak is impossible to detect. In order to obtain a detectable resonance curve, quality factor should be 15000 for the parameters given in Table 6.3. The

simulation result of the $1\mu\text{m}$ -long nanowire array resonators with $Q=15000$ is given in Fig.6.3 resonance curve of which reflects an amplitude of 2.04dB.

Table 6.3 Nanowire resonator parameters for $1\mu\text{m}$ -long nanowire array simulations

Parameter	NW 1	NW 2	NW 3	NW4	Unit
Length of the resonator, L	1	1	1	1	μm
Width of the resonator, W	28	26	24	22	nm
Height of the resonator, h	28	26	24	22	nm
Electrode to resonator gap, d	50	50	50	50	nm
DC bias, V_{DC}	20	20	20	20	V
Quality factor, Q	75	75	75	75	-
Electrode width, W_e	1	1	1	1	μm
R^*	7.5069	5.8113	4.2112	2.6147	$\text{M}\Omega$
L^*	0.4227	0.3521	0.2762	0.1869	H
C^*	0.001333	0.001854	0.002769	0.004860	fF

*Calculated from the formulation and code given in Appendix A

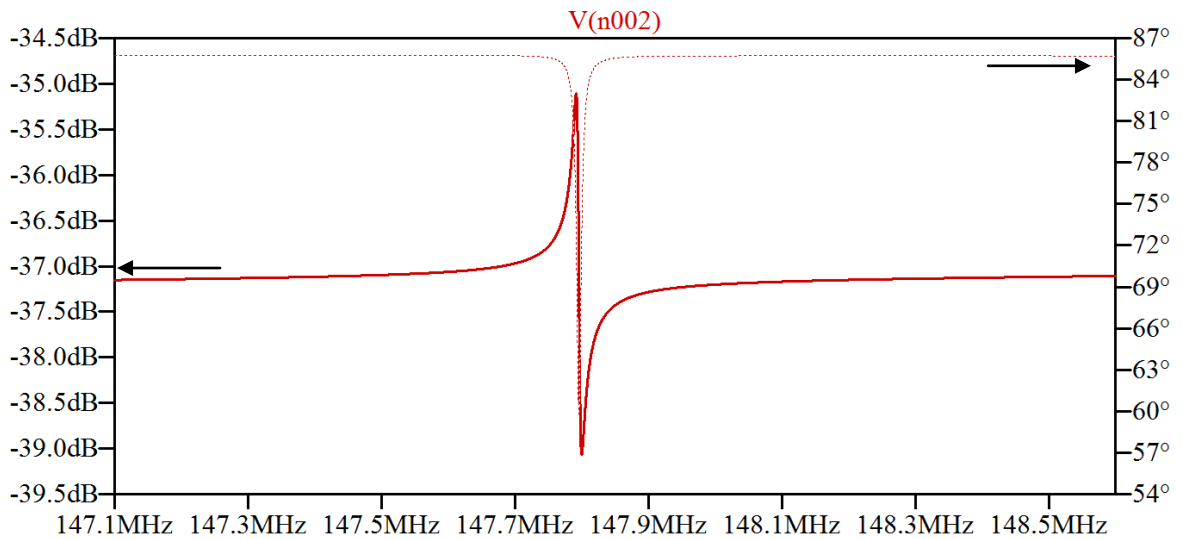


Fig.6.3 SPICE equivalent circuit model signal output of $1\mu\text{m}$ -long nanowire array resonators with $Q=15000$.

In order to increase the operation frequency, the lengths of nanowires are further decreased to 750nm. For coupled array resonators the operation frequency becomes 190 MHz. The parameters of this array are given in Table 6.4. For these parameters, a

resonance peak of amplitude 0.771dB was observed. For $Q=750$, this amplitude increases to 4.16dB.

Table 6.4 Nanowire resonator parameters for 750nm-long nanowire array simulations.

Parameter	NW 1	NW 2	NW 3	NW4	Unit
Length of the resonator, L	750	750	750	750	nm
Width of the resonator, W	28	26	24	22	nm
Height of the resonator, h	28	26	24	22	nm
Electrode to resonator gap, d	50	50	50	50	nm
DC bias, V_{DC}	50	50	50	50	V
Quality factor, Q	75	75	75	75	-
Electrode width, W_e	750	750	750	750	nm
R^*	1.3305	0.7682	0.2560	0.01604	M Ω
L^*	0.0422	0.0262	0.0095	6.467×10^{-4}	H
C^*	0.004242	0.007893	0.02591	0.4471	fF

* Calculated from the formulation and code given in Appendix A.

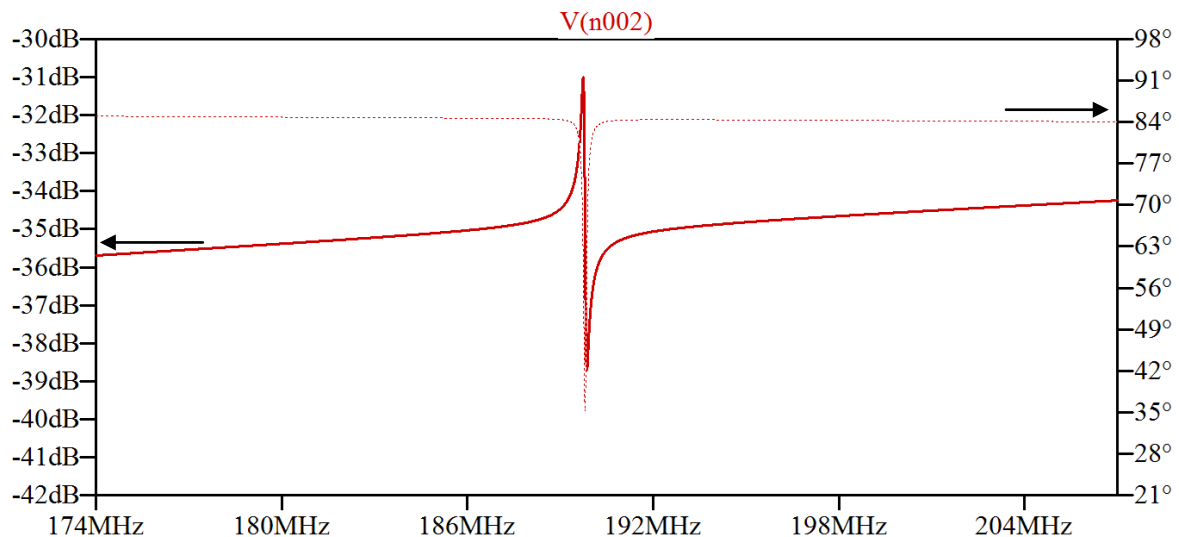


Fig.6.4 SPICE equivalent circuit model signal output of 750nm-long nanowire array resonators with $Q=750$.

The last set of nanowires investigated for signal is 500nm-long nanowire array resonators. These nanowires have highest operation frequency, 425 MHz for coupled

arrays. Ambient detection with $Q=75$ is also infeasible for this array. For this reason the simulations carried out for $Q=1500$ assuming measurement under vacuum conditions. For this case the resonance peak amplitude is shown to be 4.66dB (Fig.6. 5).

Table 6.5 Nanowire resonator parameters for 500nm-long nanowire array simulations

Parameter	NW 1	NW 2	NW 3	NW4	Unit
Length of the resonator, L	500	500	500	500	nm
Width of the resonator, W	28	26	24	22	nm
Height of the resonator, h	28	26	24	22	nm
Electrode to resonator gap, d	50	50	50	50	nm
DC bias, V_{DC}	110	110	110	110	V
Quality factor, Q	75	75	75	75	-
Electrode width, W_e	500	500	500	500	nm
R^*	0.964	0.571	0.234	0.0240	$M\Omega$
L^*	137×10^{-4}	87×10^{-4}	39×10^{-4}	4.32×10^{-4}	H
C^*	0.00263	0.00477	0.0125	0.1334	fF

* Calculated from the formulation and code given in Appendix A.

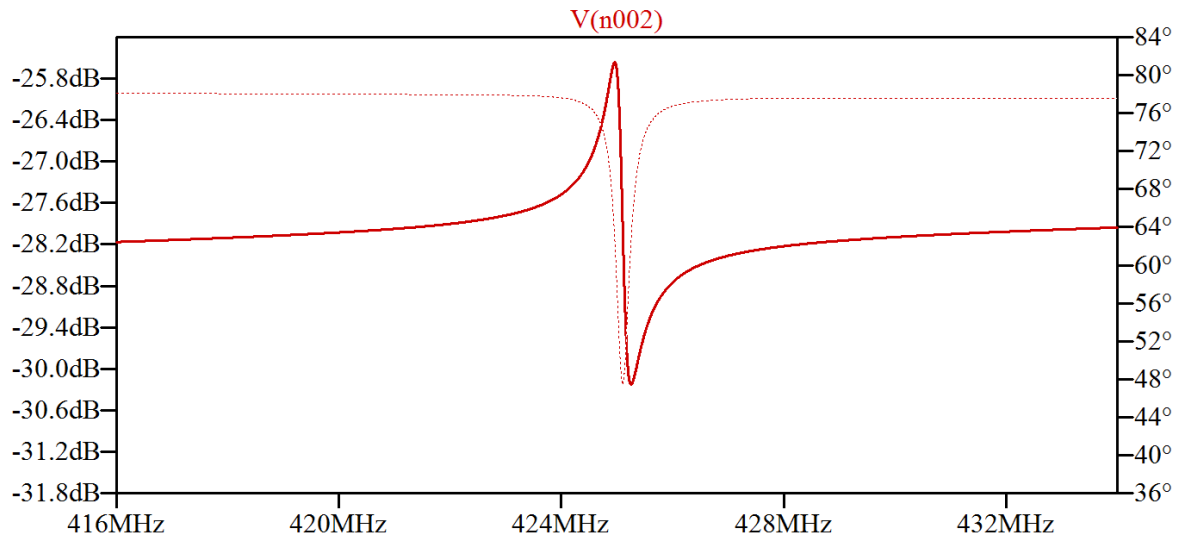


Fig.6. 5 SPICE equivalent circuit model signal output of 500nm-long nanowire array resonators with $Q=1500$.

Appendix A

Calculation of Equivalent Circuit Parameters

Equivalent electrical RLC values are needed to simulate the signal level for our nanomechanical resonator. Bannon *et. al.* had a similar approach for their filter design[48]. In this study the actuation and detection method implemented is the same and geometry is similar, we followed their calculations. In the above mentioned study, the resonator makes out of plane motion with respect to the substrate unlike nanowire resonators studied in this thesis doing in plane motion. Depending on this similarity, it is intended to find the RLC equivalents of mechanical properties of our resonator following same analysis steps.

In Fig. A.1, cross-sectional schematic of the clamped-clamped beam resonator is shown. Equivalent mass given at location y on the resonator is

$$m_r(y) = \frac{KE_{tot}}{(1/2)(v(y))^2} = \frac{\rho W_r h \int_0^{L_r} [X_{mode}(y')]^2 dy'}{[X_{mode}(y)]^2} \quad \text{A.1,}$$

where X_{mode} is the bending shape and given as:

$$X_{mode}(y) = \zeta(\cos ky - \cosh ky) + (\sin ky - \sinh ky) \quad \text{A.2,}$$

where, $k = 4.730/L_r$ and $\zeta = -1.01781$ for the fundamental mode. KE_{tot} is the peak kinetic energy of the system, $v(y)$ is the velocity at location y and dimensional parameters are given in Fig. A.1. Equivalent stiffness is given by

$$k_r(y') = \omega_0^2 m_r(y) \quad \text{A.3,}$$

where ω_0 is the radian resonance frequency of the beam.

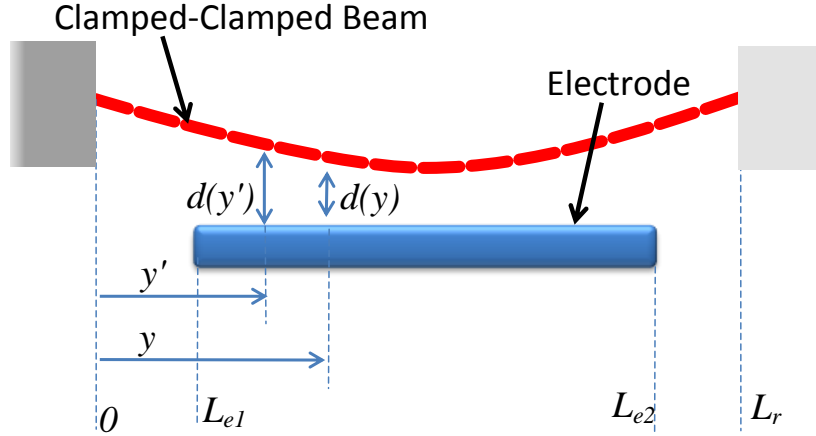


Fig. A.1 Resonator cross-sectional schematic for frequency pulling and impedance analysis.

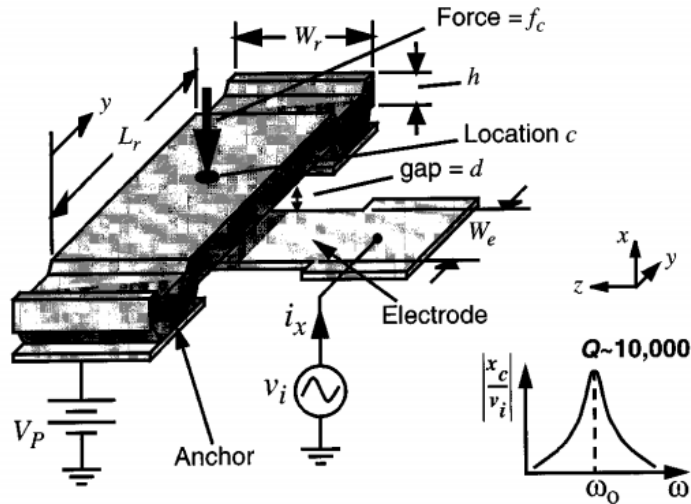


Fig. A.2 Clamped-clamped beam micromechanical resonator typical excitation configuration[48].

Electromechanical transform of R, L and C are given as $R_x = \frac{\sqrt{k_{re}m_{re}}}{Q\eta e^2} = \frac{c_{re}}{\eta e^2}$, $L_x = \frac{m_{re}}{\eta e^2}$, $C_x = \frac{\eta e^2}{k_{re}}$ where k is the stiffness, m the effective mass, Q the quality factor, c the damping factor and finally η the electromechanical transduction factor. In these entities, r denotes the resonator and e denotes the electrode location at the very center of the beam. (Fig. A.2) In our current geometry of the device, the electrode already spans the beam length but we keep this notation. (Fig. A.2) The electromechanical transduction factor is given as

$$\eta_e = \sqrt{\int_{L_{e1}}^{L_{e2}} \int_{L_{e1}}^{L_{e2}} \frac{V_P (\epsilon_0 W_r)^2}{[d(y')d(y)]^2} \frac{k_{re}}{k_r(y')} \frac{X_{mode}(y)}{X_{mode}(y')} dy dy'} \quad \text{A.4}$$

In this equation, V_P is the dc bias, ϵ_0 the permittivity of free space and $d(y)$ the gap distance of the resonator along the nanowire and is given as

$$d(y) = d_0 - \frac{1}{2} V_P^2 \epsilon_0 W_r \int_{L_{e1}}^{L_{e2}} \frac{1}{k_m(y') [d(y')]^2} \frac{X_{mode}(y)}{X_{mode}(y')} dy' \quad \text{A.5}$$

where d_0 is the static electrode to resonator gap with $V_P = 0V$. The second term represents the static displacement of the resonator towards the electrode at a particular location of y . Since $d(y)$ appears in the both sides of the equation, $d(y)$ is solved by first assuming $d(y) = d_0$ on the right side, and solving $d(y)$ on the left, then using this function again on the right and iterating until it converges.

Rearranging η by substituting equations A.1 and A3 we obtain

$$\eta_e^2 = \frac{k_{re} V_P^2 (\epsilon_0 W_r)^2}{\omega_0^2 \rho W_r h} \int_{L_{e1}}^{L_{e2}} \frac{X_{mode}(y)}{[d(y)]^2} \int_{L_{e1}}^{L_{e2}} \frac{X_{mode}(y')}{[d(y')]^2} \int_0^{L_r} \frac{1}{X_{mode}(y'') dy''} dy dy' \quad \text{A.6}$$

Once equation A.6 is solved, it is possible to calculate R,L and C values using k_{re} and m_{re} . The calculation of RLC using MATLAB code is based on these equations.

MATLAB Code

```

% the code to calculate eta,R,L,C for EM analogies.
% it utilizes the functions Dofyy and Dofy respectively
% The reason to write these functions seperately rather than to do
% function handle is that there arises some problems regarding to the
% operations like multiplication of functions. This way we call these
% functions and operate them as they are called as arrays.

%---Geometry specifics---
clc
clear all
close all
clock
L=1.8*10^(-6);%Length of the resonator
Wr=28*10^(-9);% width of the resonator,
h=28*10^(-9); % height of the resonator,
gap=50*10^(-9); % static resonator to electrode gap
Vp= 5; % dc bias
Q=75; %Q factor of the resonator
stp=10^(-6); % step size of the array generated
We=500*10^(-9); %width of the electrode
Le1=0.5*(L-We); %electrode length initial
Le2=0.5*(L+We); %electrode length final. see geometry
y=0:stp:L;
%---Constants---
j=-1.01781; %this constant is for fundamental mode
k=4.73/L;
rho=2330;% density of the SiNW (kg/m^3)
s=L/2; % the position of the measurement from 0 to L.
epsi=8.85*10^(-12); %permittivity of the free space as farad/meter
beta=4.73; %for doubly clamped beam
E=169*10^9;%Young's modulus
Area=h*Wr; %crossection area
I= (h*Wr^3)/12; % moment of inertia for this geometry
% Wo= (beta^2/L^2)*((E*I)/(rho*Area))^0.5; %fundamental frequency.
Wo=2*pi*63*10^6; % estimated by FEM simulation
%-----
Xmode=@(y) (j*(cos(k*y) - cosh(k*y)) + (sin(k*y) - sinh(k*y)));
Xmode2=@(y) (j*(cos(k*y) - cosh(k*y)) + (sin(k*y) - sinh(k*y))).^2;
ms=quadl (Xmode,Le1,Le2); %integrals
m= quadl (Xmode2,0,L)
mr=(rho*Wr*h)*m/Xmode2(L)
kre= (Wo^2)*mr
% since the effect of iteration is dominant in the results
% we dont mind if we use quad above rather than my own numeric integral
b=@(y) ((j*(cos(k*y) - cosh(k*y)) + (sin(k*y) - sinh(k*y)))./Dofy(y).^2);
int= quadl(b,Le1,Le2);

etasqr= ((kre*Vp^2*(epsi^2)*Wr)/((Wo^2)*rho*h))*(1/m)*int*int;

eta=sqrt(etasqr)
R=sqrt(kre*mr)/(etasqr*Q)
L=mr/etasqr
C=etasqr/kre
clock

```

```

%MATLAB code above to calculate RLC calls the function
%below to calculate d(y)

function d = Dofy(y); % Constants we might want to change
%---Geometry specifics---
L= 1.8*10^(-6); %Length of the resonator
Wr=28*10^(-9); % width of the resonator,
h=28*10^(-9); % height of the resonator,
gap=50*10^(-9); % static resonator to electrode gap
Vp= 5; % dc bias
Q=75; %Q factor of the resonator
stp=10^(-7); % step size of the array generated
We=500*10^(-9); %width of the electrode
Le1=0.5*(L-We); %electrode length initial
Le2=0.5*(L+We); %electrode length final. see geometry
    %y=0:stp:L;
%---Constants---
j=-1.01781; %this constant is for fundamental mode
k=4.73/L;
rho=2330; % density of the SiNW (kg/m^3)
s=L/2; % the position of the measurement from 0 to L.
epsi=8.85*10^(-12); %permittivity of the free space as farad/meter
beta=4.73; %for doubly clamped beam
E=169*10^9; %Young's modulus
Area=h*Wr;
I= (h*Wr^3)/12; % moment of inertia for this geometry
% Wo= (beta^2/L^2)*sqrt((E*I)/(rho*Area)); %fundamental frequency.
Wo=2*pi*63*10^6;
%-----
Xmode=@(y) (j*(cos(k*y)- cosh(k*y))+(sin(k*y)-sinh(k*y)));
Xmode2=@(y) (j*(cos(k*y)- cosh(k*y))+(sin(k*y)-sinh(k*y))).^2;
ms=quad (Xmode,0,L);
m= quad (Xmode2,0,L);
mr=(rho*Wr*h)*m/Xmode2(L/2);
kre= (Wo^2)*mr;
%-----d of y with first iteration-----
int=0;
int1=0;
dd=0;
for i=1:200
    for zz=0:stp:L;
        ms=[Xmode(zz)];
        if ms == 0;
            int1=int1;
        else
            int1=int1+Xmode(zz)^2;
        end
    end
    for zz=Le1:stp:Le2;
        ms=[Xmode(zz)];
        if ms == 0;
            int=int;
        else
            int=int+Xmode(zz);
        end
    end
    if i==1;
        int2=0;
        for z=Le1:stp:Le2;

```

```

        if z == 0;
            int2=int2;
        else
            int2= int2 + Xmode(z)./((Dofyy(z)).^2);
        end
    end
    dd=(gap-(((0.5*Vp^2*epsi)/(Wo^2*rho*h))*(1/int1)*int2)*Xmode(y));
else
    for z=Lel:stp:Le2;
        ind=1;
        if z == 0;
            int2=int2;
        else
            int2= int2 + Xmode(z)./(dd(ind)).^2;
        end
        ind=ind+1;
    end
    dd=gap-(((0.5*Vp^2*epsi)/(Wo^2*rho*h))*(1/int1)*int2).*Xmode(y);
end
end
d=[dd];
%hold on
%plot(y,d,'--') % top lot the distance vs. gap values
end

```

%The function Dofy(y) calls the function Dofyy(y) to have a %d(y) iterated first time by d0 as following the instruction of %paper, Bannon et.al.

```

function dd = Dofyy(y)
% The first iteration by hand is here
%-----Geometry specifics---
L=1.8*10^(-6);%Length of the resonator
Wr=28*10^(-9);% width of the resonator,
h=28*10^(-9); % height of the resonator,
gap=50*10^(-9); % static resonator to electrode gap
Vp= 5; % dc bias
Q=75; %Q factor of the resonator
stp=10^(-7); % step size of the array generated
We= 500*10^(-9); %width of the electrode
Lel=0.5*(L-We); %electrode length initial
Le2=0.5*(L+We); %electrode length final. see geometry
%---Constants---
j=-1.01781; %this constant is for fundamental mode
k=4.73/L;
rho=2330;% density of the SiNW (kg/m^3)
s=L/2; % the position of the measurement from 0 to L.
epsi=8.85*10^(-12); %permittivity of the free space as farad/meter
beta=4.73; %for doubly clamped beam
E=169*10^9;%Young's modulus
Area=h*Wr;
I= (h*Wr^3)/12; % moment of inertia for this geometry
%Wo= (beta^2/L^2)*((E*I)/(rho*Area))^0.5; %fundamental frequency.
Wo=2*pi*63*10^6; %fundamental frequency inputed from COMSOL
%-----
Xmode=@(y) (j*(cos(k*y)- cosh(k*y))+ (sin(k*y)-sinh(k*y)));
Xmode2=@(y) (j*(cos(k*y)- cosh(k*y))+ (sin(k*y)-sinh(k*y))).^2;
ms=quad (Xmode,0,L);

```

```
m= quad (Xmode2,0,L);
mr=(rho*Wr*h) *m/Xmode2 (L/2);
kre= (Wo^2) *mr;
%-----d of y with first iteration-----
int=0;
int1=0;
for zz=0:stp:L;
    ms=[ Xmode (zz)];
    if ms == 0;
        int1=int1;
    else
        int1=int1+ Xmode (zz)^2;
    end
end
for zz=Le1:stp:Le2;
    ms=[ Xmode (zz)];
    if ms == 0;
        int=int;
    else
        int=int+ Xmode (zz);
    end
end
dd=(gap- ((0.5*Vp^2*epsi) / (Wo^2*rho*h*gap^2)) *Xmode (y) *int*(1/int1));
end
```


Appendix B

COMSOL Multiphysics: Electrostatic Module Simulations

Feed through capacitances and the electrode to resonator capacitances needed for a more realistic model is calculated using the COMSOL Multiphysics: Electrostatic module. For electrode to resonator capacitance calculation an electrode and a resonator are drawn having designed specifications (Fig.B.1). After the geometry is drawn including *Air* and *SiO₂* substrate (Fig.B.1), the boundary conditions (BCs) of resonator is chosen as *Port* and the BCs of the electrode is chosen as *Ground* (Fig.B.2). On the *Port* page *Energy Method* is selected from input property list. The boundary between air and SiO₂ becomes *Continuity*. The rest of the boundaries become *Zero Charge-Symmetry*. After meshing and solving the result of capacitance calculation is obtained from *Postprocessing* menu choosing *Data display > Global*. Typing *C11_emes* in the *Expression* edit field, the value of capacitance appears in the message log at the screen (Fig.B.2).

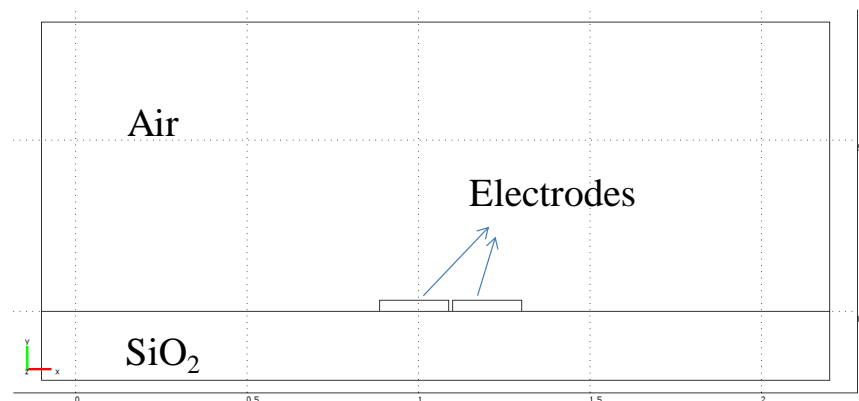


Fig.B.1 Cross-sectional view of the structures drawn in COMSOL for capacitance simulation.

A similar approach is used for the calculation of feed through capacitances (C_F). However, there are more parameters involving the calculation of C_F . Basically, we estimated fringing capacitance between electrodes. In order to calculate only the fringing capacitance between the electrodes, the adjacent parallel boundaries were also chosen to be *Zero Charge-Symmetry*. The other entire BCs configuration is the same as the electrode to resonator capacitance calculation. Choosing this configuration prevents the addition of unwanted capacitance between parallel surfaces.

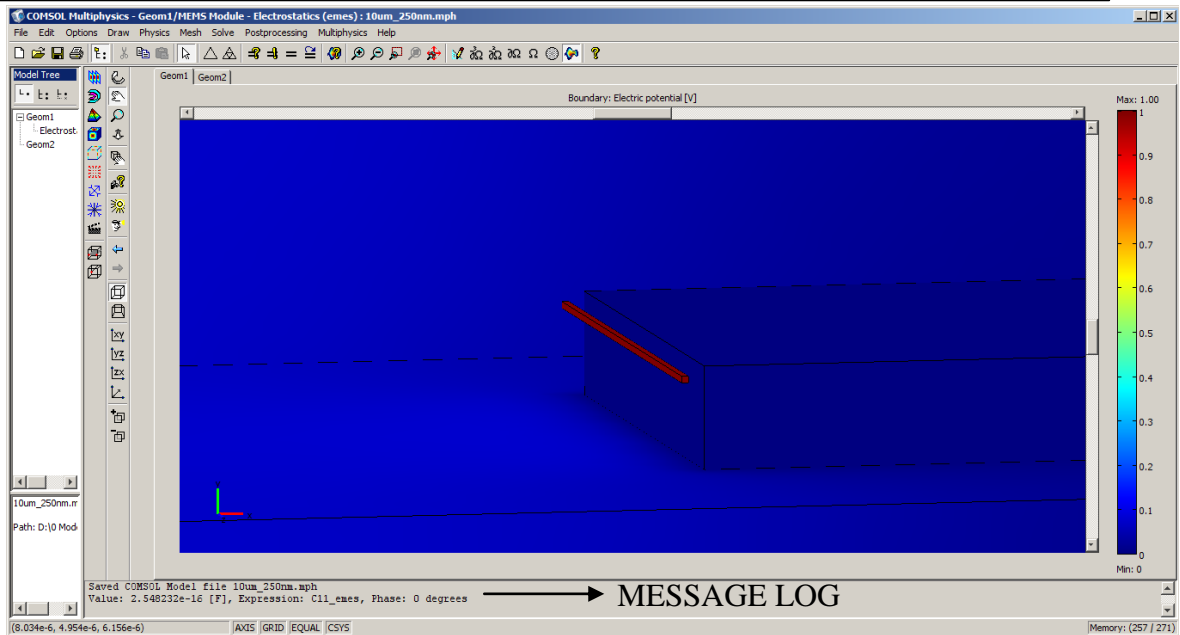


Fig.B.2 COMSOL screen print for calculation of electrode to resonator capacitance.

For the case of $1.8\mu\text{m}$ long nanowire resonators, electrodes have 128nm distance. For the procedure and configuration explained above, the electrode to electrode fringe capacitance is calculated to be 0.225fF . However, there are some other capacitances contributing to C_F . The fringe field due to the probes is estimated to be dominant with respect to the electrode fringe fields. For the schematic shown in Fig.B.3, a typical configuration of two probes is demonstrated. In this configuration, the probe wires are chosen to be $50\mu\text{m}$ in diameters, and 10cm long touching to the pads $200\mu\text{m}$ apart from each other and making 30° angle with respect to the substrate. The fringing capacitance of this system is calculated by COMSOL as 297.7 fF . Thus, the contribution of probe fringe fields is dominant to the feed through capacitances. This way, it is demonstrated that the electrode configuration do not contribute much to the C_F . For this reason, C_F is input as 300fF for the equivalent circuit simulations.

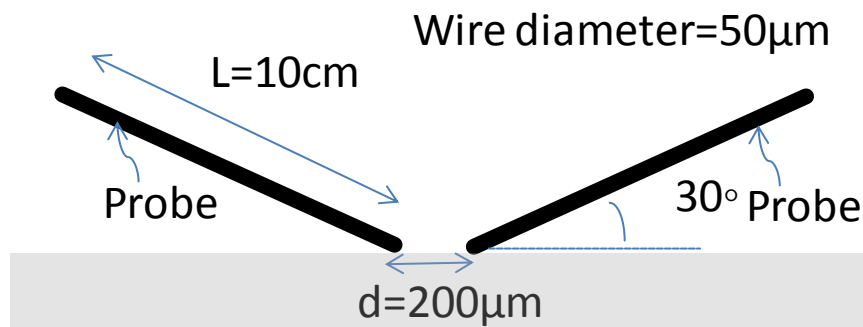


Fig.B.3 A typical configuration of probes during the measurements.

BIBLIOGRAPHY

1. C. T. C. Nguyen, "MEMS technology for timing and frequency control," *Ieee Transactions on Ultrasonics Ferroelectrics and Frequency Control* **54**, 251-270 (2007).
2. W.-T. Hsu, "Recent Progress in silicon MEMS oscillators," in *40th Annual Precise Time and Time Interval (PTTI) Meeting*(Virginia , USA, 2008), pp. pp. 135-145
3. J. T. M. van Beek, and R. Puers, "A review of MEMS oscillators for frequency reference and timing applications," *Journal of Micromechanics and Microengineering* **22**, 35 (2012).
4. H. C. Nathanson, and R. A. Wickstrom, "A Resonant-Gate Silicon Surface Transistor With High-Q Band-Pass Properties," *Applied Physics Letters* **7**, 84-86 (1965).
5. W. E. Newell, "Miniaturization of Tuning Forks," *Science* **161**, 1320-1326 (1968).
6. J. Williamson, "An overview of MEMS based timing devices," (*MEMS Investor Journal*, 2011).
7. R. A. Johnson, *Mechanical Filters in Electronics* (Wiley, 1983).
8. J. Chaste, A. Eichler, J. Moser, G. Ceballos, R. Rurali, and A. Bachtold, "A nanomechanical mass sensor with yoctogram resolution," *Nature Nanotechnology* **7**, 300-303 (2012).
9. D. W. Carr, S. Evoy, L. Sekaric, H. G. Craighead, and J. M. Parpia, "Measurement of mechanical resonance and losses in nanometer scale silicon wires," *Applied Physics Letters* **75**, 920-922 (1999).
10. H. Krommer, A. Erbe, A. Tilke, S. Manus, and R. H. Blick, "Nanomechanical resonators operating as charge detectors in the nonlinear regime," *Europhysics Letters* **50**, 101-106 (2000).
11. D. Galayko, A. Kaiser, L. Buchailot, B. Legrand, D. Collard, and C. Combi, "Design, realization and testing of micro-mechanical resonators in thick-film silicon technology with postprocess electrode-to-resonator gap reduction," *Journal of Micromechanics and Microengineering* **13**, 134-140 (2003).
12. E. Quevy, B. Legrand, D. Collard, L. Buchailot, and I. Ieee, "Ultimate technology for micromachining of nanometric gap HF micromechanical resonators," in *Mems-03: Ieee the Sixteenth Annual International Conference on Micro Electro Mechanical Systems*(2003), pp. 157-160.
13. M. Tabib-Azar, M. Nassirou, R. Wang, S. Sharma, T. I. Kamins, M. S. Islam, and R. S. Williams, "Mechanical properties of self-welded silicon nanobridges," *Applied Physics Letters* **87**, 3 (2005).
14. A. Sampathkumar, T. W. Murray, and K. L. Ekinici, "Photothermal operation of high frequency nanoelectromechanical systems," *Applied Physics Letters* **88** (2006).
15. S. S. Verbridge, L. M. Bellan, J. M. Parpia, and H. G. Craighead, "Optically driven resonance of nanoscale flexural oscillators in liquid," *Nano Letters* **6**, 2109-2114 (2006).
16. X. L. Feng, R. R. He, P. D. Yang, and M. L. Roukes, "Very high frequency silicon nanowire electromechanical resonators," *Nano Letters* **7**, 1953-1959 (2007).
17. B. Ilic, S. Krylov, L. M. Bellan, and H. G. Craighead, "Dynamic characterization of nanoelectromechanical oscillators by atomic force microscopy," *Journal of Applied Physics* **101** (2007).
18. J. M. Nichol, E. R. Hemesath, L. J. Lauhon, and R. Budakian, "Displacement detection of silicon nanowires by polarization-enhanced fiber-optic interferometry," *Applied Physics Letters* **93**, 3 (2008).

19. R. R. He, X. L. Feng, M. L. Roukes, and P. D. Yang, "Self-transducing silicon nanowire electromechanical systems at room temperature," *Nano Letters* **8**, 1756-1761 (2008).
20. M. Belov, N. J. Quitariano, S. Sharma, W. K. Hiebert, T. I. Kamins, and S. Evoy, "Mechanical resonance of clamped silicon nanowires measured by optical interferometry," *Journal of Applied Physics* **103** (2008).
21. E. Colinet, C. Durand, L. Duraffourg, P. Audebert, G. Dumas, F. Casset, E. Ollier, P. Ancey, J. F. Carpentier, L. Buchailot, and A. M. Ionescu, "Ultra-Sensitive Capacitive Detection Based on SGMOSFET Compatible With Front-End CMOS Process," *Ieee Journal of Solid-State Circuits* **44**, 247-257 (2009).
22. E. Mile, G. Jourdan, I. Bargatin, S. Labarthe, C. Marcoux, P. Andreucci, S. Hentz, C. Kharrat, E. Colinet, and L. Duraffourg, "In-plane nanoelectromechanical resonators based on silicon nanowire piezoresistive detection," *Nanotechnology* **21** (2010).
23. S. T. Bartsch, A. Lovera, D. Grogg, and A. M. Ionescu, "Nanomechanical Silicon Resonators with Intrinsic Tunable Gain and Sub-nW Power Consumption," *Acs Nano* **6**, 256-264 (2012).
24. E. F. Arkan, D. Sacchetto, I. Yildiz, Y. Leblebici, and B. E. Alaca, "Monolithic integration of Si nanowires with metallic electrodes: NEMS resonator and switch applications," *Journal of Micromechanics and Microengineering* **21**, 9 (2011).
25. R. Zhu, D. Q. Wang, S. Q. Xiang, Z. Y. Zhou, and X. Y. Ye, "Zinc oxide nanowire electromechanical oscillator," *Sensors and Actuators a-Physical* **154**, 224-228 (2009).
26. I. De Vlaminck, J. Roels, D. Taillaert, D. Van Thourhout, R. Baets, L. Lagae, and G. Borghs, "Detection of nanomechanical motion by evanescent light wave coupling," *Applied Physics Letters* **90**, 3 (2007).
27. M. A. Khaderbad, Y. Choi, P. Hiralal, A. Aziz, N. Wang, C. Durkan, P. Thiruvengathan, G. A. J. Amaratunga, V. R. Rao, and A. A. Seshia, "Electrical actuation and readout in a nanoelectromechanical resonator based on a laterally suspended zinc oxide nanowire," *Nanotechnology* **23** (2012).
28. J. L. Lopez, J. Verd, J. Teva, G. Murillo, J. Giner, F. Torres, A. Uranga, G. Abadal, and N. Barniol, "Integration of RF-MEMS resonators on submicrometric commercial CMOS technologies," *Journal of Micromechanics and Microengineering* **19** (2009).
29. A. Koumela, D. Mercier, V. Gouttenoire, C. Marcoux, S. T. Purcell, and L. Duraffourg, "Silicon nanowire resonator with integrated electrostatic actuation," *Eurosensors Xxv* **25** (2011).
30. J. Sulkko, M. A. Sillanpaa, P. Hakkinen, L. Lechner, M. Helle, A. Fefferman, J. Parpia, and P. J. Hakonen, "Strong Gate Coupling of High-Q Nanomechanical Resonators," *Nano Letters* **10**, 4884-4889 (2010).
31. L. Sekaric, D. W. Carr, S. Evoy, J. M. Parpia, and H. G. Craighead, "Nanomechanical resonant structures in silicon nitride: fabrication, operation and dissipation issues," *Sensors and Actuators a-Physical* **101**, 215-219 (2002).
32. K. L. Ekinci, "Electromechanical transducers at the nanoscale: Actuation and sensing of motion in nanoelectromechanical systems (NEMS)," *Small* **1**, 786-797 (2005).
33. A. N. Cleland, and M. L. Roukes, "Fabrication of high frequency nanometer scale mechanical resonators from bulk Si crystals," *Applied Physics Letters* **69**, 2653-2655 (1996).
34. R. G. Knobel, and A. N. Cleland, "Nanometre-scale displacement sensing using a single electron transistor," *Nature* **424**, 291-293 (2003).

35. P. A. Truitt, J. B. Hertzberg, C. C. Huang, K. L. Ekinici, and K. C. Schwab, "Efficient and sensitive capacitive readout of nanomechanical resonator arrays," *Nano Letters* **7**, 120-126 (2007).
36. Q. P. Unterreithmeier, E. M. Weig, and J. P. Kotthaus, "Universal transduction scheme for nanomechanical systems based on dielectric forces," *Nature* **458**, 1001-1004 (2009).
37. X. L. Feng, M.H. Matheny, R.B. Karabalin, C.A. Zorman, M. Mehregany, and M. L. Roukes, "Silicon Carbide (SiC) Top-Down Nanowire Electromechanical Resonators," (2009), pp. 2246 - 2249.
38. W. Y. Fung, E. N. Dattoli, and W. Lu, "Radio frequency nanowire resonators and in situ frequency tuning," *Applied Physics Letters* **94** (2009).
39. Q. P. Unterreithmeier, T. Faust, S. Manus, and J. P. Kotthaus, "On-Chip Interferometric Detection of Nanomechanical Motion," *Nano Letters* **10**, 887-890 (2010).
40. D. Karabacak, T. Kouh, C. C. Huang, and K. L. Ekinici, "Optical knife-edge technique for nanomechanical displacement detection," *Applied Physics Letters* **88** (2006).
41. A. Husain, J. Hone, H. W. C. Postma, X. M. H. Huang, T. Drake, M. Barbic, A. Scherer, and M. L. Roukes, "Nanowire-based very-high-frequency electromechanical resonator," *Applied Physics Letters* **83**, 1240-1242 (2003).
42. M. U. Demirci, and C. T. C. Nguyen, "Mechanically corner-coupled square microresonator array for reduced series motional resistance," *Journal of Microelectromechanical Systems* **15**, 1419-1436 (2006).
43. S. Pourkamali, and F. Ayazi, "Electrically coupled MEMS bandpass filters - Part 1: With coupling element," *Sensors and Actuators a-Physical* **122**, 307-316 (2005).
44. J. R. Clark, F. D. Bannon, A. C. Wong, C. T. C. Nguyen, and Ieee, "Parallel-resonator HF micromechanical bandpass filters," *Transducers 97 - 1997 International Conference on Solid-State Sensors and Actuators, Digest of Technical Papers, Vols 1 and 2*, 1161-1164 (1997).
45. K. Wang, C. T. C. Nguyen, and Ieee, "High-order micromechanical electronic filters," in *IEEE 10th Annual International Workshop on Micro Electro Mechanical Systems*(Nagoya, Japan, 1997), pp. 25-30.
46. K. Wang, and C. T. C. Nguyen, "High-order medium frequency micromechanical electronic filters," *Journal of Microelectromechanical Systems* **8**, 534-557 (1999).
47. C. T.-C. Nguyen, and R. T. Howe, "Q-Controlled Microresonators and Tunable Electronic Filters Using Such Resonators," (2001).
48. F. D. Bannon, J. R. Clark, and C. T. C. Nguyen, "High-Q HF microelectromechanical filters," *Ieee Journal of Solid-State Circuits* **35**, 512-526 (2000).
49. S. Lee, and C. T. C. Nguyen, "Mechanically-coupled micromechanical resonator arrays for improved phase noise," *Proceedings of the 2004 Ieee International Frequency Control Symposium and Exposition*, 144-150 (2005).
50. S. S. Li, M. U. Demirci, Y. W. Lin, Z. Ren, and C. T. C. Nguyen, "Bridged micromechanical filters," in *IEEE International Frequency Control Symposium and Exposition*(Montreal, CANADA, 2004), pp. 280-286.
51. W.-T. Hsu, "Micromechanical Resonator Having Short Support Beams," (Discera, 2005).
52. M. U. Demirci, C. T. C. Nguyen, and Ieee, "A low impedance VHF micromechanical filter using coupled-array composite resonators," *Transducers '05, Digest of Technical Papers, Vols 1 and 2*, 2131-2134 (2005).

53. S. S. Li, Y. W. Lin, Z. Y. Ren, C. T. C. Nguyen, and Ieee, "Disk-array design for suppression of unwanted modes in micromechanical composite-array filters," in *19th IEEE International Conference on Micro Electro Mechanical Systems (MEMS 2006)*(Istanbul, TURKEY, 2006), pp. 866-869.
54. M. Motiee, R. R. Mansour, and A. Khajepour, "Novel MEMS filters for on-chip transceiver architecture, modeling and experiments," *Journal of Micromechanics and Microengineering* **16**, 407-418 (2006).
55. J. Giner, A. Uranga, F. Torres, E. Marigo, and N. Barniol, "Fully CMOS integrated bandpass filter based on mechanical coupling of two RF MEMS resonators," *Electronics Letters* **46**, 640-U659 (2010).
56. C. T.-C. Nguyen, and S.-S. Li, "High Q Micromechanical Resonator Devices and Filters Utilizing Same," (The Regents of the University of Michigan, 2007).
57. Y. W. Lin, L. W. Hung, S. S. Li, Z. Y. Ren, C. T. C. Nguyen, and Ieee, "Quality factor boosting via mechanically-coupled arraying," *Transducers '07 & Eurosensors Xxi, Digest of Technical Papers, Vols 1 and 2, U1235-U1236* (2007).
58. M. Lutz, A. Partridge, and Z. Pan, "MEMS Resonator Array Structure and Method of Operating and Using Same," (Robert Bosch GmbH, 2007).
59. Y. Lin, W. C. Li, B. Kim, Y. W. Lin, Z. Y. Ren, C. T. C. Nguyen, and Ieee, "Enhancement of Micromechanical Resonator Manufacturing Precision Via Mechanically-Coupled Arraying," *2009 Joint Meeting of the European Frequency and Time Forum and the Ieee International Frequency Control Symposium, Vols 1 and 2, 58-63* (2009).
60. Z. Pan, R. N. Candler, M. Lutz, A. Partridge, V. Materna, G. Yama, and W. Frey, "In-Plane Mechanically Coupled Microelectromechanical Tuning Fork Resonators," (2008).
61. C. Kharrat, and E. Colinet, "Array of Coupled Resonators Bandpass Filter and Oscillator," (2010).
62. A. Hashimura, "MEMS Filter Device Having a Nanosize Coupling Element and Manufacturing Method Thereof," P. Corporation, ed. (2010).
63. M. A. Hopcroft, W. D. Nix, and T. W. Kenny, "What is the Young's Modulus of Silicon?," *Journal of Microelectromechanical Systems* **19**, 229-238 (2010).
64. H. C. Harrison, "Acoustic Device," U. P. Office, ed. (1929).
65. H. A. C. Tilmans, "Equivalent circuit representation of electromechanical transducers .1. Lumped-parameter systems (vol 6, pg 157, 1996)," *Journal of Micromechanics and Microengineering* **6**, 359-359 (1996).
66. A. Bloch, "Electromechanical Analogies and Their Use for the Analysis of Mechanical and Electromechanical Systems," *Journal of the Institution of Electrical Engineers*, 157-169 (1945).
67. F. Laermer, and A. Schilp, "Method of Anisotropic Etching of Silicon," (Robert Bosch GmbH, 2003).